

Spurious Aeroacoustic Emissions in Lattice Boltzmann Simulations on Non-Uniform Grids

Alexander Schukmann ^{1,†} , Viktor Haas ¹ and Andreas Schneider ^{2,*}

¹ Department of Mechanical and Process Engineering, University of Kaiserslautern-Landau, 67663 Kaiserslautern, Germany; alexander.schukmann@volkswagen.de (A.S.); vhaas@rptu.de (V.H.)

² Department of Mechanical and Process Engineering, Offenburg University, 77652 Offenburg, Germany

* Correspondence: andreas.schneider@hs-offenburg.de

† Current address: CFD Method Development, Volkswagen AG, 38440 Wolfsburg, Germany.

Abstract: Although there do exist a few aeroacoustic studies on harmful artificial phenomena related to the usage of non-uniform Cartesian grids in lattice Boltzmann methods (LBM), a thorough quantitative comparison between different categories of grid arrangement is still missing in the literature. In this paper, several established schemes for hierarchical grid refinement in lattice Boltzmann simulations are analyzed with respect to spurious aeroacoustic emissions using a weakly compressible model based on a D3Q19 athermal velocity set. In order to distinguish between various sources of spurious phenomena, we deploy both the classical Bhatnagar–Gross–Krook and other more recent collision models like the hybrid recursive-regularization operator, the latter of which is able to filter out detrimental non-hydrodynamic mode contributions, inherently present in the LBM dynamics. We show by means of various benchmark simulations that a cell-centered approach, either with a linear or uniform explosion procedure, as well as a vertex-centered direct-coupling method, proves to be the most suitable with regards to aeroacoustics, as they produce the least amount of spurious noise. Furthermore, it is demonstrated how simple modifications in the selection of distribution functions to be reconstructed during the communication step between fine and coarse grids affect spurious aeroacoustic artifacts in vertex-centered schemes and can thus be leveraged to positively influence stability and accuracy.

Keywords: lattice Boltzmann method; local grid refinement; aeroacoustics; spurious noise



Academic Editor: Markus Klein

Received: 27 December 2024

Revised: 22 January 2025

Accepted: 25 January 2025

Published: 28 January 2025

Citation: Schukmann, A.; Haas, V.; Schneider, A. Spurious Aeroacoustic Emissions in Lattice Boltzmann Simulations on Non-Uniform Grids. *Fluids* **2025**, *10*, 31. <https://doi.org/10.3390/fluids10020031>

Copyright: © 2025 by the authors. Licensee MDPI, Basel, Switzerland. This article is an open access article distributed under the terms and conditions of the Creative Commons Attribution (CC BY) license (<https://creativecommons.org/licenses/by/4.0/>).

1. Introduction

With the lattice Boltzmann method (LBM) gaining ever more popularity among computational fluid dynamics (CFD) and computational aeroacoustics (CAA) practitioners over the last few decades, several techniques for local grid refinement tailored to the method have been developed in order to satisfy the need for economical usage of computational resources. It is well known, however, that grid transition interfaces (GTIs) exhibiting abrupt variations in spatial resolution and various interpolation procedures, typical for non-uniform Cartesian grids used in the LBM, act as a source of spurious numerical artifacts accompanied by severe negative effects on the stability and accuracy of a simulation [1–5].

A widely recognized category of grid refinement techniques takes advantage of the standard collide and stream procedure of the LBM as well as its efficient application on Cartesian grids by hierarchically subdividing the grid cells in a quad- (2D) or octree (3D) like manner, maintaining integer length and time scale ratios between neighboring grid levels. Depending on the data structure and specific arrangement of coarse and fine grid nodes relative to one another, this approach manifests itself in the form of various layouts,

all of which generally utilize some sort of interpolation in order to reconstruct missing information during communication between the fine and coarse grids. A schematic depiction of established GTI layouts is shown in Figure 1 for two dimensions. Whereas vertex-centered (vc) algorithms are characterized by grid nodes residing in cell corners and thus partially co-located coarse and fine nodes along grid transition interfaces, cf. Figure 1a,b, cell-centered (cc) methods apply a volumetric description without the possibility of co-location [6], cf. Figure 1c.

In the vc framework, missing information at nodes with a co-located partner node on the neighboring level can be transferred from this partner through rescaling of its non-equilibrium distribution functions [7,8], while missing distribution functions at hanging nodes—i.e., those without a co-located partner node—are reconstructed employing spatial interpolation, usually based on cubic polynomials. Synchronization between grid levels is ensured by temporal interpolation. Typically, a grid overlap is used [9–12], allowing for a stability-enhancing explicit filtering of fine non-equilibrium functions to be applied during fine-to-coarse communication [13,14]. A vertex-centered grid structure including an *overlap* between grids will be referred to as vc-ov within the course of this paper.

A more recent vc algorithm proposed by Astoul et al. [4] omits overlapping and transferring complete sets of distribution functions at co-located nodes from their respective partners. Instead, missing fine and coarse distribution functions at these nodes are reconstructed simultaneously by requiring zeroth- and first-order non-equilibrium moments to vanish, which is achieved by iterative determination of a consistent equilibrium function. Distribution functions at hanging nodes are then reconstructed similarly to vc-ov. This *direct-coupling* approach will be referred to as vc-dc.

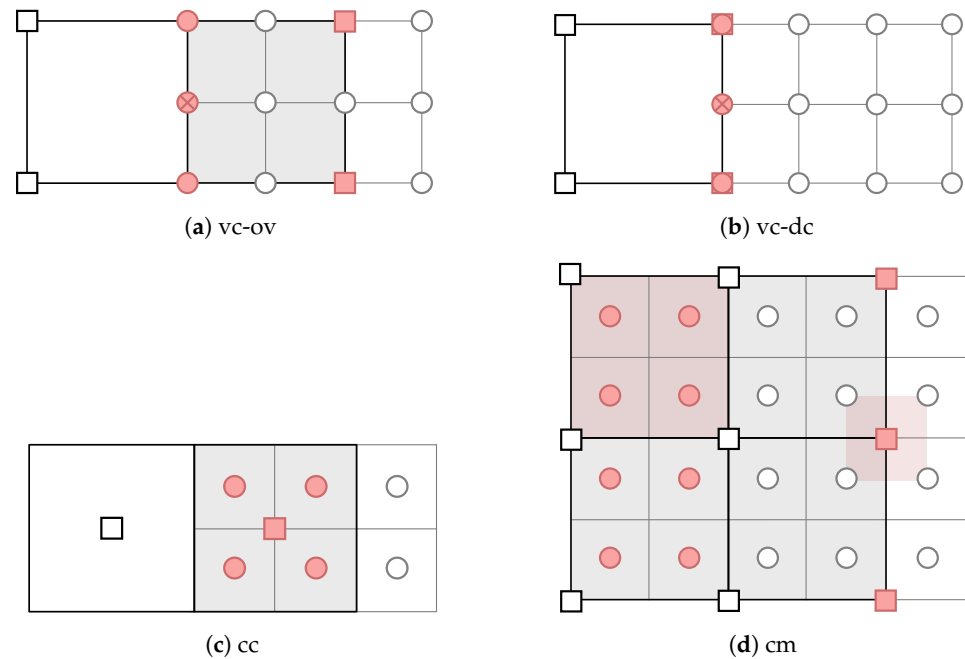


Figure 1. Schematic representation of GTI variants investigated in this work, depicted in 2D for simplicity. vc-ov: vertex-centered with grid overlap, vc-dc: vertex-centered with direct grid coupling (no overlap), cc: cell-centered, cm: combined. Gray coarse cells indicate the extent of the grid overlap. The two light red cells in (d) exemplarily mark the validity range of the local bubble functions. ●: fine interface node (with coarse partner in case of vc), ○: regular fine node, ■: coarse interface node (with fine partner in case of vc), □: regular coarse node, ⊗: hanging node.

In order to refill fine states after streaming in cc algorithms, coarse post-collision states are exploded onto fine interface nodes either uniformly [15] or by employing linear

interpolation [16]. Missing coarse states are obtained by averaging fine particle densities, which is known as coalescence and acts as an implicit filtering operation during fine-to-coarse communication [2,17]. Since two layers of interface nodes need to be supplied with distribution functions and are thus able to perform two subsequent fine streaming steps, temporal interpolation becomes unnecessary. Furthermore, no rescaling of non-equilibrium distribution functions is performed when transferring information from one grid to another.

Another type of arrangement arises when both grids are shifted relative to each other with coarse nodes sitting in the coarse cell corners and fine nodes residing in their respective cell centers [18,19], cf. Figure 1d. Following a previous study by the authors [5], this kind of grid layout will be referred to as a *combined* approach (cm) in the remainder of this paper. Reconstruction of missing distribution functions on both grids is achieved by gradient-based compact spatial interpolation. Similarly to cc algorithms, no temporal interpolation takes place. However, rescaling of non-equilibrium functions is applied, meaning that this approach literally combines operations of both vc and cc algorithms.

Since vortical pressure and density fluctuations are typically several orders of magnitude stronger than their purely acoustic counterparts, minor errors in the transmission and reconstruction of information, as well as sudden changes in cell size over GTIs, can lead to unphysical disturbances, which may appear unproblematic with regard to aerodynamic evaluation or perhaps remain undetected but would significantly distort simulation results from a point of view of aeroacoustics. Such spurious acoustic artifacts have been long known and reported in investigations utilizing classical Navier–Stokes-based solvers [20–27] and somewhat more recently for the LBM [2–4,28,29] and are categorized in numerical reflections of acoustic waves at GTIs as well as numerical noise generated by vorticity passing through GTIs. A detailed and comprehensive literature review for classical Navier–Stokes-based solvers in this regard can be found, e.g., in chapter 5 of [30] or for the LBM in chapter 6 of [31]. Apart from the mentioned types of numerical noise, harmful interactions between non-hydrodynamic modes inherently present in the LBM dynamics and GTIs can act as spurious acoustic sources and lead to instabilities that render any LBM simulation null and void [3]. Even if stability is not affected, this poses a serious difficulty in direct aeroacoustic simulations, which can be effectively performed with the LBM due to its ability to recover the Navier–Stokes equations in the weakly compressible limit and thus capture both unsteady aerodynamics as well as acoustic wave propagation simultaneously while exhibiting low dissipative properties [32–37].

Interestingly, to the best of the authors' knowledge, direct comparisons between LBM grid refinement algorithms in the context of spurious aeroacoustic artifacts are only sparsely covered in the literature. This is especially the case for different interface layouts, cf. Figure 1. In [2], Gendre et al. conducted a comparison between their *directional splitting* approach and the refinement algorithm of Lagrava [13,14] in terms of an acoustic pulse and a convected vortex crossing a refinement interface. Both of these algorithms are based on a vertex-centered arrangement. An extensive comparison of vertex-centered algorithms was later presented in the PhD thesis of Astoul [31]. The introduced vertex-centered *direct coupling* method in combination with the hybrid-recursive regularization collision model (HRR) [38] proved to perform superior with regards to the eradication of numerical noise.

With respect to comparisons between different types of grid layouts, only a single qualitative result could be identified by the authors in the literature and is included in Section 2 of [3], where Figure 2, showing a vortex passing through a refinement interface, indicates an increased amount of artificial noise produced by the cell-centered algorithm with linear explosion [16] compared with the Lagravas vertex-centered algorithm mentioned above.

The present paper, which is a continuation of our previous work [5], where different grid refinement algorithms and collision operators were analyzed with respect to their

stability and accuracy, attempts to close part of this gap by analyzing the various grid refinement algorithms displayed in Figure 1 with regards to the amount of numerical noise generated. For this purpose, four test cases of significance for aeroacoustics and with increasing complexity are examined, namely a 2D Gaussian acoustic pulse, a 1D convected acoustic wave, a 2D convected barotropic vortex, and finally a 3D jet flow. We show that for all four numerical test cases performed, a cell-centered approach, either with linear or uniform interpolation during the explode procedure, as well as a vertex-centered direct-coupling method, proves to be the most suitable with regards to aeroacoustics, as they produce the least amount of spurious noise. At this point, it should be mentioned that we only focus on refinement methods that are based on the classical collide-and-stream algorithm and which we consider to be representative for the majority of lattice Boltzmann simulations with local grid refinement.

After a concise recap of the theoretical background, collision models, boundary conditions, and the necessary terminology regarding the analyzed grid refinement schemes in Section 2, we continue with a discussion of the conducted numerical tests and their respective results in Section 3. Finally, we close this work with a summary and outlook on future work in Section 4.

To conclude this introductory part, we would like to highlight the above-mentioned numerical artifacts associated with the change in local grid size by an illustrative example. Due to the existence of vortical structures with a variety of spatial and temporal scales as well as a substantial presence of non-hydrodynamic modes, such spurious effects are particularly noticeable in high Reynolds number turbulent flows, as relevant for many engineering applications. Figure 2 shows a large eddy simulation of the airflow around a generic side mirror mounted on a flat plate [39] at two different Reynolds numbers, $Re = 5.2 \times 10^5$ and $Re = 1.1 \times 10^5$, and a Mach number of $Ma = 0.1$ using the LBM with a D3Q19 velocity stencil and hybrid-recursive regularization collision operator. The hybridization factor in the HRR model was set to $\sigma = 0.98$ as recommended in [31] for high Reynolds number turbulent flows. No explicit (i.e., based on physical reasoning) subgrid-scale stress model was used, leading to an implicit SGS formulation utilizing the HRR model's inherent dissipation for the treatment of underresolved scales. The spatial discretization of the flow domain was realized by a non-uniform Cartesian grid consisting of several levels with the highest resolution, i.e., the smallest grid size, enclosing the object and a total number of approximately 2×10^8 grid nodes. As the highly turbulent wake emerging from the plate and blunt body surfaces and indicated by means of contours of the Q -criterion passes through the innermost GTI located downstream, the GTI acts as a source of artificial acoustic waves, clearly visible as disturbances in the grayscaled velocity divergence field. These disturbances are propagated upstream, superimposing the physical sound field in the region around the body and thus distorting any aeroacoustic evaluation, especially in the case of the higher Reynolds number.

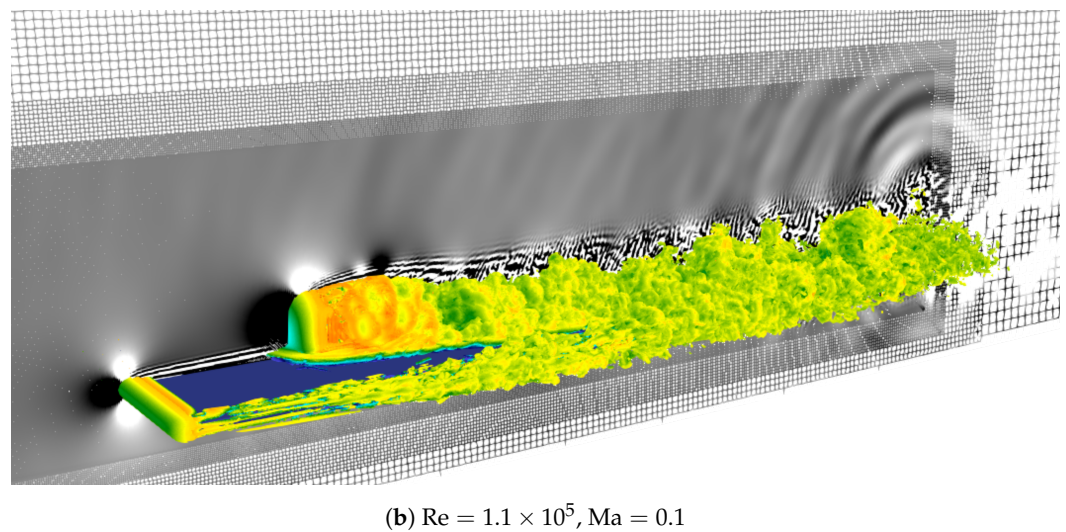
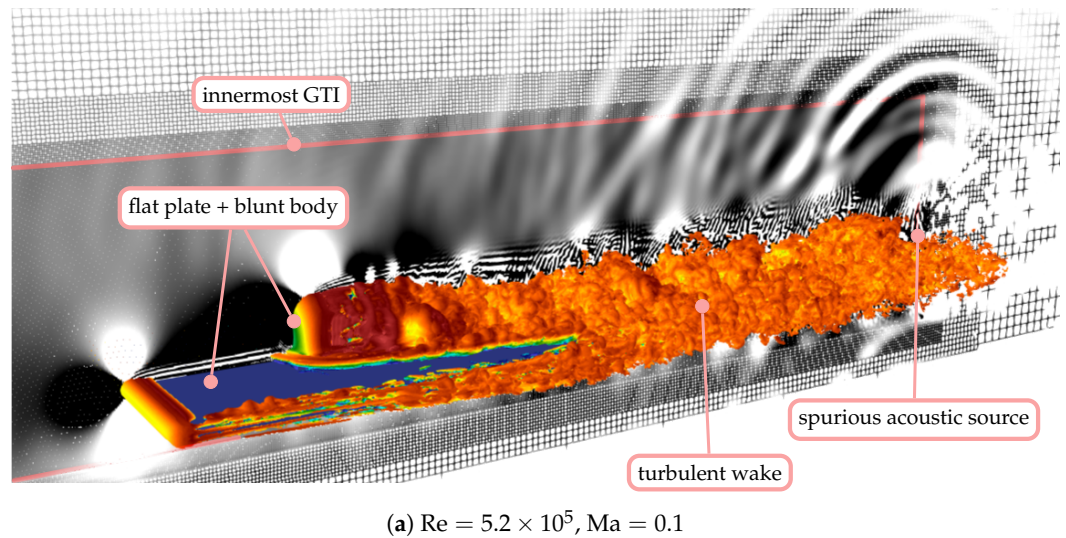


Figure 2. Lattice Boltzmann simulation of a low Mach number airflow over a blunt body mounted on a flat plate at two different Reynolds numbers. Spurious acoustic waves visualized as disturbances in velocity divergence $\nabla \cdot \mathbf{u}$ (grayscale) are emitted from the downstream grid transition interface (GTI). The turbulent wake is visualized by Q -criterion and colored by velocity magnitude.

2. Overview of Methods

2.1. Lattice Boltzmann Method

The lattice Boltzmann equation (LBE) (1) describes the spatiotemporal evolution of a discrete set of distribution functions f_i representing phase-space densities of fictitious particles, typically solved for on a Cartesian grid with spacing Δx and involving a restriction of velocity space such that the particles travel with a velocity ξ_i from one grid node to selected neighbors during one time step Δt . The left-hand side of the LBE reflects this node-to-node particle transport, while the right-hand side describes local particle redistribution by means of collision operator $\Omega_i(\mathbf{x}, t)$:

$$f_i(\mathbf{x} + \xi_i \Delta t, t + \Delta t) - f_i(\mathbf{x}, t) = \Omega_i(\mathbf{x}, t). \tag{1}$$

Figure 3 shows the two common D2Q9 and D3Q19 velocity sets or lattices. The D3Q19 set represents the basis of all numerical experiments discussed in Section 3, whereas the D2Q9 set is used for its simplicity in order to review and clarify concepts regarding the different

grid layouts in Section 2.5. With the *molecular velocity* $\tilde{\xi} = \frac{\Delta x}{\Delta t}$, particle velocity vectors for the D3Q19 lattice are given by

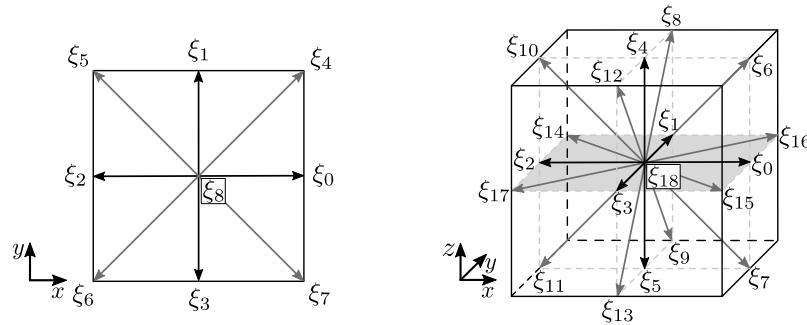


Figure 3. Discrete velocity sets for D2Q9 and D3Q19 lattices [5].

$$\tilde{\xi}_i = \begin{cases} (0, 0, 0) & i = 18 \\ (\pm\tilde{\xi}, 0, 0), (0, \pm\tilde{\xi}, 0), (0, 0, \pm\tilde{\xi}) & i = 0, \dots, 5 \\ (\pm\tilde{\xi}, \pm\tilde{\xi}, 0), (\pm\tilde{\xi}, 0, \pm\tilde{\xi}), (0, \pm\tilde{\xi}, \pm\tilde{\xi}) & i = 6, \dots, 17. \end{cases} \quad (2)$$

Macroscopic physical quantities are extracted from the mesoscopic scale as moments of the distribution function. In discretized phase space, these moments are evaluated as weighted sums using Gauss–Hermite quadrature with discrete particle velocities as abscissae [40], yielding $M(x, t) = \sum_{i=0}^{q-1} \varphi(\tilde{\xi}_i) f_i$, where $f_i = w_i f(x, \tilde{\xi}_i, t)$. Herein, f describes a polynomial expansion of the phase space continuous velocity distribution function [41]. For the D3Q19 lattice, the quadrature weights w_i results in [42]

$$w_i = \begin{cases} \frac{1}{3}, & i = 18 \\ \frac{1}{18}, & i = 0, \dots, 5 \\ \frac{1}{36}, & i = 6, \dots, 17. \end{cases} \quad (3)$$

The relationship between the molecular velocity $\tilde{\xi}$ and the isothermal speed of sound $c_s = p/\rho = \sqrt{RT}$ is then given by $\tilde{\xi} = \sqrt{3}c_s$.

2.2. Bhatnagar–Gross–Krook Collision Model

The classical collision model introduced by Bhatnagar, Gross, and Krook in 1954 [43] represents an approximation of particle collision by $\Omega^{\text{BGK}} = -1/\tau(f - f^{eq})$, i.e., relaxing the velocity distribution function f towards the Maxwell–Boltzmann equilibrium distribution $f^{eq}(\rho, \mathbf{u}, \boldsymbol{\xi}) = \rho/(2\pi c_s^2)^{\frac{3}{2}} \exp(-(\boldsymbol{\xi}-\mathbf{u})^2/2c_s^2)$ by means of a single relaxation time τ . Adapted to the LBE, the discrete form of the BGK approximation is given by

$$\Omega_i^{\text{BGK}} = -\frac{\Delta t}{\tau + \frac{1}{2}\Delta t} (f_i - f_i^{(0)}) = -\frac{c_s^2 \Delta t}{\nu + \frac{1}{2}c_s^2 \Delta t} (f_i - f_i^{(0)}) = -\tilde{\omega} f_i^{neq}, \quad (4)$$

where f_i and $f_i^{(0)}$ replace their respective continuous equivalents f and f^{eq} and with $\tilde{\omega}$ being the so-called dimensionless collision frequency. Regarding the discrete equilibria $f_i^{(0)}$, we rely on the following third-order Hermite polynomial expansion form:

$$\begin{aligned}
 f_i^{(0)} = w_i \left[\sum_{n=0}^2 \frac{1}{c_s^{2n} n!} \mathcal{H}_i^{(n)} : \mathbf{A}_0^{(n)} + \frac{1}{2c_s^6} \left(\mathcal{H}_{i,xxxy}^{(3)} + \mathcal{H}_{i,yzz}^{(3)} \right) \left(A_{0,xxxy}^{(3)} + A_{0,yzz}^{(3)} \right) \right. \\
 + \frac{1}{2c_s^6} \left(\mathcal{H}_{i,xxz}^{(3)} + \mathcal{H}_{i,yyz}^{(3)} \right) \left(A_{0,xxz}^{(3)} + A_{0,yyz}^{(3)} \right) \\
 + \frac{1}{2c_s^6} \left(\mathcal{H}_{i,xyy}^{(3)} + \mathcal{H}_{i,xzz}^{(3)} \right) \left(A_{0,xyy}^{(3)} + A_{0,xzz}^{(3)} \right) \\
 + \frac{1}{6c_s^6} \left(\mathcal{H}_{i,xxxy}^{(3)} - \mathcal{H}_{i,yzz}^{(3)} \right) \left(A_{0,xxxy}^{(3)} - A_{0,yzz}^{(3)} \right) \\
 + \frac{1}{6c_s^6} \left(\mathcal{H}_{i,xxz}^{(3)} - \mathcal{H}_{i,yyz}^{(3)} \right) \left(A_{0,xxz}^{(3)} - A_{0,yyz}^{(3)} \right) \\
 \left. + \frac{1}{6c_s^6} \left(\mathcal{H}_{i,xyy}^{(3)} - \mathcal{H}_{i,xzz}^{(3)} \right) \left(A_{0,xyy}^{(3)} - A_{0,xzz}^{(3)} \right) \right], \quad (5)
 \end{aligned}$$

including orthogonalized third-order Hermite moments in order to get rid of spurious couplings among them [38,44]. Due to its insufficient quadrature order, isotropic Hermite tensors of the form $\mathcal{H}_{i,\alpha\alpha\alpha}^{(3)}$ or $\mathcal{H}_{i,\alpha\beta\gamma}^{(3)}$ have to be excluded for the D3Q19 lattice [45,46].

Hermite equilibrium expansion coefficients $A_0^{(n)}$ in Equation (5) are obtained through a projection of the Maxwell–Boltzmann equilibrium distribution onto a n^{th} -order Hermite polynomial basis, defined as [3]

$$\mathcal{H}_i^{(n)} = \frac{(-c_s^2)^n}{\omega(\xi_i)} \nabla_{\xi}^n \omega(\xi_i) \quad \text{with} \quad \omega(\xi) = \frac{1}{(2\pi c_s^2)^{\frac{3}{2}}} \exp\left(-\frac{\|\xi\|_2^2}{2c_s^2}\right), \quad (6)$$

with ∇_{ξ}^n expressing the n^{th} -order gradient with respect to ξ . These expansion coefficients are related to or directly coincide with equilibrium moments and are given by [46]

$$\begin{aligned}
 A_0^{(0)} &= \rho, \\
 A_{0,\alpha}^{(1)} &= \rho u_{\alpha}, \\
 A_{0,\alpha\beta}^{(2)} &= \rho u_{\alpha} u_{\beta} + \rho c_s^2 \delta_{\alpha\beta}, \\
 A_{0,\alpha\beta\gamma}^{(3)} &= \rho u_{\alpha} u_{\beta} u_{\gamma} \delta_{\alpha\beta}, \quad \text{where} \quad \delta_{\alpha\beta} = \begin{cases} 1, & \alpha = \beta \\ 0, & \alpha \neq \beta \end{cases}. \quad (7)
 \end{aligned}$$

2.3. Regularized Collision Models

Since the presence of non-hydrodynamic modes in the BGK model is known to cause serious stability issues, especially due to detrimental interactions with grid interfaces [3,4], we employ regularized collision operators to emphasize and investigate these effects. Besides their filtering and damping capabilities regarding non-hydrodynamic modes, regularized models offer another decisive advantage with respect to aeroacoustics in that they do not increase bulk viscosity [31] to improve stability, as is often the case with many common multiple-relaxation time models [2]. The core idea behind regularized models consists of abandoning terms of order $n > 1$ contained within the non-equilibria in Equation (4), i.e., approximating $f_i^{neq} = f_i - f_i^{(0)}$ by $f_i^{neq} \simeq f_i^{(1)}$ and thus relying on explicit reconstruction of the first-order non-equilibrium part $f_i^{(1)}$ [47,48]. These abandoned terms correspond to high-order physics, not correctly representable on standard lattices like the D3Q19. As the target physics of such LBMs lies within the range of Navier–Stokes level hydrodynamics (first-order truncation of the Knudsen number expansion of f), keeping

only the first-order non-equilibria is a reasonable approximation. The LBE then takes the following form:

$$f_i(\mathbf{x} + \boldsymbol{\xi}_i \Delta t, t + \Delta t) = f_i^{(0)} + (1 - \tilde{\omega}) f_i^{(1)}. \tag{8}$$

Similar to the equilibrium functions $f_i^{(0)}$ and $f_i^{(1)}$ are reconstructed through Hermite series expansion, including orthogonal third-order non-equilibrium moments in order to deal with spurious couplings among them [38,44]:

$$\begin{aligned} f_i^{(1)} = w_i \left[\frac{1}{2c_s^4} \mathcal{H}_i^{(2)} : A_1^{(2)} + \frac{1}{2c_s^6} \left(\mathcal{H}_{i,xx}^{(3)} + \mathcal{H}_{i,yy}^{(3)} \right) \left(A_{1,xx}^{(3)} + A_{1,yy}^{(3)} \right) \right. \\ + \frac{1}{2c_s^6} \left(\mathcal{H}_{i,xz}^{(3)} + \mathcal{H}_{i,yz}^{(3)} \right) \left(A_{1,xz}^{(3)} + A_{1,yz}^{(3)} \right) \\ + \frac{1}{2c_s^6} \left(\mathcal{H}_{i,xy}^{(3)} + \mathcal{H}_{i,xz}^{(3)} \right) \left(A_{1,xy}^{(3)} + A_{1,xz}^{(3)} \right) \\ + \frac{1}{6c_s^6} \left(\mathcal{H}_{i,xx}^{(3)} - \mathcal{H}_{i,yy}^{(3)} \right) \left(A_{1,xx}^{(3)} - A_{1,yy}^{(3)} \right) \\ + \frac{1}{6c_s^6} \left(\mathcal{H}_{i,xz}^{(3)} - \mathcal{H}_{i,yz}^{(3)} \right) \left(A_{1,xz}^{(3)} - A_{1,yz}^{(3)} \right) \\ \left. + \frac{1}{6c_s^6} \left(\mathcal{H}_{i,xy}^{(3)} - \mathcal{H}_{i,xz}^{(3)} \right) \left(A_{1,xy}^{(3)} - A_{1,xz}^{(3)} \right) \right]. \tag{9} \end{aligned}$$

Notice the tensor contraction involving only second-order contributions, due to zeroth- and first-order terms being equal to zero in our case, cf. e.g., Section 2.3 in [5]. Non-equilibrium expansion coefficients $A_1^{(2)}$ are obtained by projection of the non-equilibrium functions onto the second-order Hermite tensor [45], cf. Equation (6), whereas higher-order terms are calculated exploiting recurrence relations proposed in [49]. Owing to this property, the method is known as *recursive regularization* (RR). With third-order Hermite tensors expressed by means of second-order ones as $\mathcal{H}_{i,\alpha\alpha\beta}^{(3)} = (\tilde{\xi}_{i,\alpha} \tilde{\xi}_{i,\alpha} - c_s^2) \tilde{\xi}_{i,\beta}$ and by ruling out isotropic tensors $\mathcal{H}_{i,\alpha\alpha\alpha}^{(3)}$ and $\mathcal{H}_{i,\alpha\beta\gamma}^{(3)}$ as was previously performed for $f_i^{(0)}$, expansion coefficients result to

$$A_{1,\alpha\beta}^{(2)} = \sum_i \mathcal{H}_{i,\alpha\beta}^{(2)} (f_i - f_i^{(0)}) = \sum_i \left(\tilde{\xi}_{i,\alpha} \tilde{\xi}_{i,\beta} - \delta_{\alpha\beta} c_s^2 \right) f_i^{neq}, \tag{10}$$

$$A_{1,\alpha\alpha\beta}^{(3)} = 2u_\alpha A_{1,\alpha\beta}^{(2)} + u_\beta A_{1,\alpha\alpha}^{(2)}. \tag{11}$$

A further improvement regarding stability was achieved with the hybrid-recursive regularized collision operator (HRR), introduced in [38]. In this method, second-order non-equilibrium expansion coefficients $A_1^{(2)}$, which relate to the viscous stress tensor through $A_{1,\alpha\beta}^{(2)} = -2S_{\alpha\beta} \rho c_s^2 \Delta t / \tilde{\omega}$ [45], are hybridized as follows before being utilized in the reconstruction of $f_i^{(1)}$ in Equation (9):

$$A_1^{(2)} = \sigma A_1^{(2),PR} + (1 - \sigma) A_1^{(2),FD}, \quad \text{with } [0 \leq \sigma \leq 1]. \tag{12}$$

$A_1^{(2),PR}$ represents projection-based moments computed by Equation (10), whereas the second term $A_1^{(2),FD}$ is determined by approximating strain rates $S_{\alpha\beta} = \frac{1}{2}(\partial_\beta u_\alpha + \partial_\alpha u_\beta)$ contained within the stress tensor using central finite differences, yielding

$$A_{1,\alpha\beta}^{(2),FD} = -\frac{\rho c_s^2 \Delta t}{\tilde{\omega}} \left(\frac{u_\alpha(x + e_\beta \Delta x) - u_\alpha(x - e_\beta \Delta x)}{2\Delta x} + \frac{u_\beta(x + e_\alpha \Delta x) - u_\beta(x - e_\alpha \Delta x)}{2\Delta x} \right). \tag{13}$$

The RR model is recovered by setting $\sigma = 1$ in Equation (12), where $\sigma = 0$ leads to a solely finite difference-based reconstruction of the viscous stress tensor. Selecting $\sigma \in [0, 1[$, a significant stability increase can be achieved compared with the RR model by effectively damping non-hydrodynamic mode contributions [3,4,38,50,51].

2.4. Non-Reflecting Boundary Conditions

Common boundary conditions imposing density or velocity values at domain inlets or outlets inevitably cause sound wave reflections for compressible flow solvers [52], polluting the density and consequently the pressure field [53]. Since our goal is to examine numerical noise originating exclusively from the GTI, the Gaussian acoustic pulse and three-dimensional jet test case in Section 3 have been investigated utilizing so-called non-reflecting characteristic Dirichlet boundary conditions (CBCs) adapted to the LBM [54]. These shall be briefly addressed in the following.

Through a diagonalization of the Euler conservation equations, a decomposition into characteristics, typically representing acoustic waves and advective transport, is achieved, leading to the local one-dimensional inviscid (LODI) equations [55,56]. Considering in Figure 4 an exemplary computational domain with characteristic waves $\mathcal{L}_{x,1}, \mathcal{L}_{x,2}, \mathcal{L}_{x,3}, \mathcal{L}_{x,4}, \mathcal{L}_{x,5}$ entering or leaving through y - z -boundary faces and propagating at their respective velocities $u_x + c_s, u_x, u_x, u_x, u_x - c_s$, and LODI equations are given by

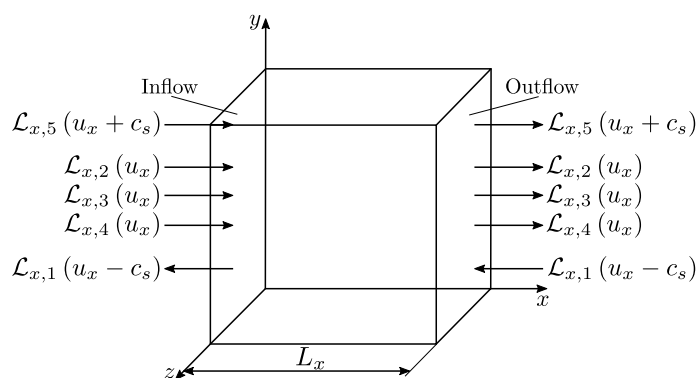


Figure 4. Amplitudes of characteristic waves at two outflow boundaries in x -direction with opposite orientation of face normal vector [55].

$$\begin{bmatrix} \partial_t \rho + \frac{1}{c_s^2} \left[\mathcal{L}_{x,2} + \frac{1}{2}(\mathcal{L}_{x,5} + \mathcal{L}_{x,1}) \right] \\ \partial_t u_x + \frac{1}{2\rho c_s} (\mathcal{L}_{x,5} - \mathcal{L}_{x,1}) \\ \partial_t u_y + \mathcal{L}_{x,3} \\ \partial_t u_z + \mathcal{L}_{x,4} \\ \partial_t p + \frac{1}{2\rho c_s} (\mathcal{L}_{x,5} + \mathcal{L}_{x,1}) \end{bmatrix} = \begin{bmatrix} 0 \\ 0 \\ 0 \\ 0 \\ 0 \end{bmatrix} \tag{14}$$

The vector of macroscopic hydrodynamic variables $\mathbf{g} = (\rho, u_x, u_y, u_z)^T$, needed for the realization of Dirichlet-type boundary conditions, is determined by ideally setting incom-

ing wave amplitudes to zero while simultaneously leaving outgoing waves undisturbed and solving the LODI Equation (14) numerically. As usual in the LBM, the calculated macroscopic quantities need to be expressed in terms of mesoscopic particle distributions to be specified at boundary nodes. For this purpose, we impose equilibrium distribution functions $f_i^{(0)}(\rho, \mathbf{u})$ computed by means of Equation (5) [37,54].

For the outflow in Figure 4 located at $x = L_x$, characteristic wave amplitude variations read [55]

$$\begin{bmatrix} \mathcal{L}_{x,1} \\ \mathcal{L}_{x,2} \\ \mathcal{L}_{x,3} \\ \mathcal{L}_{x,4} \\ \mathcal{L}_{x,5} \end{bmatrix} = \begin{bmatrix} (u_x - c_s) [c_s^2 \partial_x p - \rho c_s \partial_x u_x] \\ u_x [c_s^2 \partial_x \rho - \partial_x p] \\ u_x (\partial_x u_y) \\ u_x (\partial_x u_z) \\ (u_x + c_s) [\partial_x p - \rho c_s \partial_x u_x] \end{bmatrix} \tag{15}$$

Here, $\mathcal{L}_{x,1}$ represents sound propagation in the $-x$ direction and the only wave entering the domain through the outflow. Accordingly, $\mathcal{L}_{x,5}$ is the acoustic wave travelling in the $+x$ direction. The entropy wave $\mathcal{L}_{x,2}$ is equal to zero in the athermal case, since fluid pressure and density are related like $p = c_s^2 \rho$. The remaining two waves, $\mathcal{L}_{x,3}$ and $\mathcal{L}_{x,4}$, carry vorticity information. In order to achieve a non-reflecting pressure outflow boundary condition, the unknown incoming wave amplitude $\mathcal{L}_{x,1}$ is approximated by a pressure relaxation given as [55]

$$\mathcal{L}_{x,1} = K_1 \frac{c_s (1 - \text{Ma}^2)}{L_x} (p - p_\infty), \tag{16}$$

with p_∞ being a target pressure and Ma the maximum Mach number at the boundary. Setting the relaxation constant $K_1 = 0$ results in a perfectly non-reflecting boundary condition but is generally not preferable due to strong pressure variations rendering the method unstable [57–59]. For this reason we set $K_1 = 1$ for the Gaussian acoustic pulse and $K_1 = 1 \times 10^{-3}$ for the jet flow.

The remaining amplitudes $\mathcal{L}_{x,3}$, $\mathcal{L}_{x,4}$, and $\mathcal{L}_{x,5}$ for outgoing waves are calculated according to Equation (15), with spatial derivatives of physical quantities g being approximated using one-sided second-order finite-difference quotients with a backwards stencil:

$$(\partial_\alpha g_I)(x) \approx \frac{\mp 3g_I(x) \pm 4g_I(x \pm e_\alpha \Delta x) \mp g_I(x \pm e_\alpha 2\Delta x)}{2\Delta x}, \tag{17}$$

where upper-row arithmetic operators apply to the y - z -boundary with a positive outward-pointing normal vector at $x = L_x$. Finally, the LODI equations (14) can be solved by means of a simple forward Euler step:

$$g_I(\mathbf{x}, t + \Delta t) \approx g_I(\mathbf{x}, t) + \Delta t \partial_t g_I(\mathbf{x}, t), \tag{18}$$

providing the hydrodynamic variables to be set at the boundary in the next time iteration.

2.5. Local Grid Refinement

A detailed overview of vc-ov, cc, and cm grid refinement algorithms is given in our previous study [5], where the latter two of the three schemes have been adapted in order to allow for consistent central-difference approximation of strain rates across grid interfaces when HRR collision is employed. Regarding vc-dc, a comprehensive description can be found in [31]. Nevertheless, we would like to provide a concise summary of each individual method’s basics and establish the relevant nomenclature.

In order to keep descriptions vivid, we will restrict ourselves to one additional level of refinement, thus two neighboring grid levels with spacings connected by $\Delta x^c = 2\Delta x^f$.

Here, superscripts c and f indicate the coarse and fine grid levels, respectively. Moreover, we employ convective scaling to link time steps between levels as $\Delta t^c = 2\Delta t^f$ and to keep the molecular velocity $\tilde{\xi}$ and, as a consequence, the isothermal speed of sound c_s constant.

2.5.1. Vertex-Centered Schemes

Vertex-centered schemes are characterized by partially co-located coarse ■ and fine ● interface nodes residing in cell corners, as well as partnerless hanging nodes ⊗ in between [7,60]. Since interface nodes miss same-level neighbors in at least one direction, the respective missing post-streaming functions must be somehow provided. If a grid overlap is used (refer to Figure 1a), typically all functions at co-located nodes are reconstructed by transferring information from corresponding partners as

$$c \rightarrow f: f_i^f = f_i^{(0)} + \mathcal{R}f_i^{neq,c}, \forall i \tag{19}$$

$$f \rightarrow c: f_i^c = f_i^{(0)} + \frac{1}{\mathcal{R}}f_i^{neq,f}, \forall i, \tag{20}$$

where rescaling of f_i^{neq} by $\mathcal{R} = \bar{\omega}^c/2\bar{\omega}^f$ ensures consistency of the viscous stress tensor across grid levels. This reconstruction procedure is inserted into the core algorithm after streaming and before the collision step, following [8].

In order to remove fine scales above the Nyquist wavenumber that cannot be represented on the coarse grid, stability-enhancing filters are often explicitly applied to the non-equilibrium functions in Equation (20) in scale-resolving simulations of turbulent flows. To investigate the influence of these methods concerning spurious noise, we include restrictions according to Lagrava et al. [13] and Touil et al. [14], corresponding to a simple arithmetic mean over all lattice neighbors and an anisotropic filter, respectively, into some of our tests in Section 3. These methods will be abbreviated as LAG and TOU throughout this work. Given that other types of refinement schemes often perform such filtering implicitly [2], which is also the case for the cc and cm algorithms examined in this study, incorporating the aforementioned operations yields an equal and intriguing comparison.

The direct-coupling algorithm [4] dispenses with overlapping grids (cf. Figure 1b) and instead solves the following non-linear equation system constituting a constraint on zeroth- and first-order non-equilibrium moments in order to establish a connection between grid levels and reconstruct missing post-streaming distribution functions at co-located coarse ■ and fine ● interface nodes:

$$\sum_i \Gamma_i \Phi_i f_i^{neq, \gamma_i} = \sum_i \Gamma_i \Phi_i \left(f_i^{\gamma_i} - f_i^{(0)}(\rho, \mathbf{u}) \right) = 0, \tag{21}$$

where parameters Γ_i and γ_i can take the values $\{1, \mathcal{R}\}$ and $\{c, f\}$ depending on the specific vc-dc variant and subset, as explained down below, $\Phi_i = (1, \tilde{\xi}_{i,x}, \tilde{\xi}_{i,y}, \tilde{\xi}_{i,z})^T$ and $\mathbf{u} = (u_x, u_y, u_z)^T$ in 3D. The only unknown is the vector of macroscopic variables $(\rho, \mathbf{u})^T$, since all post-collision states on both grids are available. As for this reason, the choice of f_i to be used in Equation (21) is not unambiguous; two possible variants of the direct-coupling method are introduced in [4], both of them starting from a reconstruction at the fine level.

Distribution functions are divided into subsets, comprising the subset \mathcal{M} of missing functions, the subset \mathcal{Q} of functions known exclusively at either interface node, and the subset \mathcal{P} of functions known at both interface nodes simultaneously. If, for example, the D2Q9 lattice definition shown in Figure 3 and the vc-dc layout in Figure 1b are taken as a basis, these subsets result in $\mathcal{M}^f = \mathcal{Q}^c = \{0, 4, 7\}$, $\mathcal{Q}^f = \mathcal{M}^c = \{2, 5, 6\}$, and $\mathcal{P} = \{1, 3, 8\}$.

Summing over lattice directions i in Equation (21), missing distribution functions obviously need to be transferred from coarse partners, whereas known fine functions must be utilized, since $\mathcal{Q}^f = \mathcal{M}^c$. It is the selection of the distributions in \mathcal{P} that defines the

distinctions between the two variants of the method. In the *vc-dc1* algorithm, distribution functions belonging to \mathcal{P} are taken from the fine grid, whereas the *vc-dc2* algorithm relies on coarse functions for the determination of $f_i^{(0)}(\rho, \mathbf{u})$, in order to reduce aliasing and interpolation errors associated with functions streamed from hanging nodes \otimes . Hence, Equation (21) can be rewritten in the following form, with Γ_i and γ_i replaced by their corresponding values and the rescaling factor \mathcal{R} defined as above:

$$\sum_{i \in \mathcal{Q}^f} \Phi_i f_i^{neq,f} + \sum_{i \in \mathcal{M}^f} \mathcal{R} \Phi_i f_i^{neq,c} + \sum_{i \in \mathcal{P}} \Phi_i f_i^{neq,f} = \mathbf{0} \quad \text{for vc-dc1,} \quad (22)$$

$$\sum_{i \in \mathcal{Q}^f} \Phi_i f_i^{neq,f} + \sum_{i \in \mathcal{M}^f} \mathcal{R} \Phi_i f_i^{neq,c} + \sum_{i \in \mathcal{P}} \mathcal{R} \Phi_i f_i^{neq,c} = \mathbf{0} \quad \text{for vc-dc2.} \quad (23)$$

To determine the roots of the system, a Newton–Raphson method [61] is used, which will not be discussed in depth here. A complete description is given in [4].

With the new equilibrium distributions thus obtained, Astoul et al. firstly reconstruct $f_i^f, \forall i \in \mathcal{M}^f$ according to Equation (19) and then $f_i^c, \forall i \in \mathcal{M}^c \cup \mathcal{P}$ as per Equation (20), providing all states required for the succeeding collision step. A reconstruction of known \mathcal{P} functions is performed in order to ensure consistent treatment between grid levels and avoid potential mass and momentum conservation violation [4].

Another approach examined in Section 3 of the present paper consists of first replacing $f_i^f, \forall i \in \mathcal{M}^f \cup \mathcal{P}$ and subsequently reconstructing only $f_i^c, \forall i \in \mathcal{M}^c$, to exploit and retain as much available coarse post-streaming information as possible. In this variant, coarse functions belonging to the subset \mathcal{P} need not be reconstructed since they have already been utilized in the reconstruction of corresponding fine functions and would therefore remain unchanged.

To distinguish between these methods in Section 3, the first approach will be indicated by the suffix Mf McP, as missing fine and coarse, as well as coarse \mathcal{P} functions are replaced. Accordingly, suffix MfP Mc identifies the second variant of reconstruction.

Furthermore, we will also apply different reconstruction procedures to the *vc-ov* algorithm, named in a similar manner, i.e., with reconstructed distribution functions at either level mentioned explicitly by an appropriate suffix *only* in cases where not all states are replaced. If, for example, only missing distribution functions belonging to \mathcal{M} are reconstructed on both grids, leaving functions in \mathcal{Q} and \mathcal{P} unaffected, a consistent use of our naming convention yields *vc-ov Mf Mc*, whereas *vc-ov MfP* indicates a reconstruction of \mathcal{M}^f and fine \mathcal{P} distributions while replacing all coarse functions. For the standard approach of reconstructing all functions on both interface nodes, the suffix is dropped, giving *vc-ov*. A schematic representation of the different reconstruction variants is given in Figure A2 based on *vc-ov*.

In all *vc* schemes, distribution functions at \otimes are reconstructed by applying cubic $p(x) = \sum_{\alpha=0}^3 a_\alpha x^\alpha$ [9], and in the case of additional face-centered hanging nodes occurring in 3D, bi-cubic $p(x, y) = \sum_{\alpha=0}^3 \sum_{\beta=0}^3 a_{\alpha\beta} x^\alpha y^\beta$ [62] polynomial interpolation is used, thereby utilizing information of co-located nodes. Only states corresponding to lattice directions previously reconstructed at co-located nodes are also reconstructed at hanging nodes. Synchronization of coarse and fine distributions during reconstruction at intermediate iterations $t + \Delta t^f$ is achieved by means of linear interpolation in time [63].

2.5.2. Cell-Centered Schemes

Cell-centered schemes [6] (refer to Figure 1c) employed in this work are based on two specific grid-coupling steps. During $c \rightarrow f$ coupling, coarse post-collision distributions f_i^c

at $\blacksquare(\mathbf{x}^c, t)$ traveling towards the fine grid are redistributed among fine interface nodes $\bullet(\mathbf{x}^f, t)$ contained within the same coarse parent cell either uniformly [15]:

$$f_i^f(\mathbf{x}^f, t) = f_i^c(\mathbf{x}^c, t), \forall i \in \mathcal{M}^f, \tag{24}$$

or by relying on linear spatial interpolation of f_i^c along directions α parallel to the interface as follows [16]:

$$f_i^f(\mathbf{x}^f, t) = f_i^c(\mathbf{x}^c, t) + (\mathbf{x}^f - \mathbf{x}^c) \cdot \left(\mathbf{F}_i(\mathbf{x}^c, t) - \frac{\boldsymbol{\xi}_i(\boldsymbol{\xi}_i \cdot \mathbf{F}_i(\mathbf{x}^c, t))}{|\boldsymbol{\xi}_i|^2} \right), \forall i \in \mathcal{M}^f, \tag{25}$$

$$F_{i\alpha}(\mathbf{x}^c, t) = \frac{f_i^c(\mathbf{x}^c + e_\alpha \Delta x^c, t) - f_i^c(\mathbf{x}^c - e_\alpha \Delta x^c, t)}{2\Delta x^c}.$$

Accordingly, the procedures in Equations (24) and (25) are each referred to as *uniform* and *linear explosion* in the course of this work. Since two rows of fine interface nodes are supplied with coarse post-collision states, they remain valid for two consecutive fine time steps, thereby omitting the need for temporal interpolation.

Concerning $f \rightarrow c$ communication, *coalescence* implies missing coarse densities to be obtained by averaging fine particle densities contained within the coarse parent cell, resulting in the following expression for three spatial dimensions:

$$f_i^c(\mathbf{x}^c, t) = \frac{1}{8} \sum_{\bullet} f_i^f(\mathbf{x}^f, t), \forall i \in \mathcal{M}^c. \tag{26}$$

This procedure acts as implicit filtering of fine distributions, as a result of spatial equalization of grids [17]. Even though no explicit rescaling of distributions is occurring in the cc algorithm described here, Rohde et al. [15] assume a rescaling of the non-equilibrium part to be implicitly present in their method.

2.5.3. Combined Schemes

The combined grid arrangement can be defined as a combination of both aforementioned layouts, with fine nodes residing in their respective cell centers and being enclosed by regular coarse nodes \square sitting in the coarse parent cells corners. Similarly, coarse interface nodes \blacksquare are surrounded by regular fine cell-centered nodes \circ [17–19,37], as depicted in Figure 1d, resulting in a grid overlap of two coarse cells. Thus, missing distribution functions at interface nodes can be reconstructed by applying Equations (19) and (20) with minor modifications. Density ρ in $f_i^{(0)}$ as well as the non-equilibrium part f_i^{neq} are interpolated trilinearly, whereas for the velocity vector \mathbf{u} we apply the following second-order polynomial expression as part of a compact gradient-based interpolation scheme:

$$u_\alpha^{\mathcal{I}}(x, y, z) = a_{\alpha,000} + a_{\alpha,100}x + a_{\alpha,010}y + a_{\alpha,001}z + a_{\alpha,200}x^2 + a_{\alpha,110}xy + a_{\alpha,101}xz + a_{\alpha,020}y^2 + a_{\alpha,011}yz + a_{\alpha,002}z^2 + a_{\alpha,111}xyz, \tag{27}$$

with $\alpha = x, y, z$, and where superscript \mathcal{I} indicates an interpolated value. For details regarding the calculation of coefficients $a_{\alpha,ijk}$ in Equation (27), please refer to appendix C in [5].

As in the cc algorithm, no temporal interpolation is performed, since two layers of fine interface nodes are updated simultaneously. Furthermore, the spatial interpolation of quantities during $f \rightarrow c$ communication can be seen as a filtering procedure.

It should be mentioned that some authors classify this approach as a cell-centered method [2,37,64], cf. Figure A1. However, such a volumetric perspective entails a small

peculiarity in the order in which the reconstruction of missing functions at interface nodes is carried out: coarse interface nodes ■ must be treated before fine interface nodes ●, since the latter depend on a proper set of distribution functions of the former; cf. section 2.2 in [64]. When relying on a combined perspective, however, the order of reconstruction at interface nodes becomes arbitrary.

3. Numerical Experiments and Results

In order to emphasize the motivation for the selection of the individual benchmarks in Section 3, the following research questions may serve as guidance:

- Gaussian acoustic pulse: How do the individual refinement schemes compare with regard to the produced amount of artificial noise, given a purely acoustic scenario, i.e., without background flow?
- Convected acoustic wave: To what extent do these methods differ in terms of interactions between spurious acoustic modes and the grid refinement interface when background flow is present?
- Convected barotropic vortex: What is the effect on grid-transition-induced spurious artifacts when vorticity crosses the refinement interface?
- Three-dimensional jet flow: Do the conclusions drawn in all previous cases hold true for a more demanding, high-Reynolds number flow?

3.1. Gaussian Acoustic Pulse

The Gaussian pulse is a classical benchmark for acoustic simulations and has served as a verification tool in a number of studies in the LBM context for both uniform [65,66] and non-uniform grids [2,4,28]. In the present paper, the target of interest comprises an acoustic pulse at $Ma = 0$ that passes across a planar refinement interface, whereby a portion of the pulse is reflected. Since spurious acoustic modes are static in such a case and therefore do not interact with the interface, the observed reflections can be attributed solely to properties of the grid refinement scheme as well as the sudden change in spatial resolution [3,4].

A schematic depiction of the calculation domain comprising a pseudo-2D box of dimensions $[L, L, \Delta x^c]$ with $L = 3$ m is shown in Figure 5. To prevent unphysical reflections at boundaries from corrupting the analysis, characteristic pressure boundary conditions are defined at the boundary faces. Additionally, a sponge layer including a linear increase in viscosity up to a maximum value of $\nu = 19.05 \text{ m}^2 \text{ s}^{-1}$ separates the boundaries from the inner region. As explained in Section 2.4, we set the relaxation constant $K_1 = 1$.

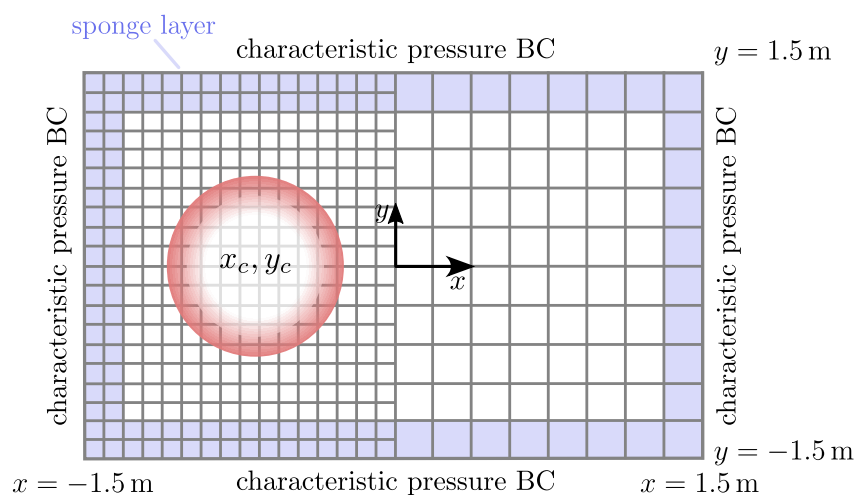


Figure 5. Schematic representation of the calculation domain for the Gaussian acoustic pulse test case.

Since sound waves typically travel from higher to lower spatial resolution in a simulation, the Gaussian pulse is initialized in the fine grid as

$$\begin{cases} \rho'(r, t = 0) = \rho_0 \epsilon \exp(-\beta r^2) & \bar{\rho} = \rho_0, \\ u'_x(r, t = 0) = 0 & \bar{u}_x = 0, \\ u'_y(r, t = 0) = 0 & \bar{u}_y = 0, \end{cases} \quad (28)$$

and crosses the grid transition located at the center of the domain. In Equation (28), perturbation quantities are defined like $\phi' = \phi - \bar{\phi}$. Furthermore, ρ_0 is the base density, ϵ the pulse amplitude, and β the shape factor, related to the standard deviation R_c through $2\beta = R_c^{-2}$ and $r = \sqrt{(x - x_c)^2 + (y - y_c)^2}$.

Although non-hydrodynamic modes remain static here, unphysical artifacts attributed to their presence may still appear with the BGK model, superimposing pulse reflections and affecting the interpretation of results. For this reason, we adopt the HRR model with a hybridization factor of $\sigma = 0.98$ for the Gaussian acoustic pulse test case, effectively damping the aforementioned non-hydrodynamic mode impact.

The chosen value for σ is recommended in [31] for high-Reynolds number turbulent flows, as they are generally found in industrial applications. Due to the ever-growing significance of scale-resolving simulations in this context and with the HRR operator's enhanced stability properties, its choice as a basis for this simple benchmark seems natural. Furthermore, as in our previous study, we adapted the HRR model with regard to a consistent central-difference approximation of strain rates across cc and cm refinement interfaces [5]; the Gaussian pulse enables us to verify our approach for acoustic scenarios.

The pulse's spatiotemporal evolution can be expressed in terms of the following analytical expression:

$$\rho'(r, t) = \frac{\rho_0 \epsilon}{2\beta} \int_0^\infty \exp(-\xi^2/4\beta) \cos(c_s t \xi) J_0(\xi r) \xi d\xi, \quad (29)$$

That was determined with the help of Wolfram Mathematica for verification and is evaluated along the abscissa in Figure 6 compared with an HRR solution on a uniform fine grid that serves as a reference. In Equation (29), $J_0(\cdot)$ represents the zeroth-order Bessel function of the first kind. All remaining relevant simulation parameters are summarized in Table 1.

Table 1. Parameter set for the Gaussian acoustic pulse.

$\Delta x^c / \text{m}$	$c_s / \text{m s}^{-1}$	$\rho_0 / \text{kg m}^{-3}$	$\nu / \text{m}^2 \text{s}^{-1}$	ϵ	R_c / m	$(x_c / \text{m}, y_c / \text{m})$
0.02	347.3	1.17621	1.49×10^{-5}	0.01	0.06	$(-8R_c, 0)$

Besides a stability increase, the injected numeric viscosity within the HRR model [38], controlled by the value of σ (cf. Figure 5.8 in [5]), leads to a significant dissipation of spurious modes [3] and expectedly affects the attenuation of physical sound waves as well. However, as depicted in Figure 7 at time $t = 80\Delta t$ for the reference solution on a uniform fine grid, the pulse's amplitude decreases relative to the BGK solution only by approximately 0.007% and 0.015% for $\sigma = 0.99$ and $\sigma = 0.98$, respectively. This aspect underlines the suitability of the HRR collision model for aeroacoustic purposes.

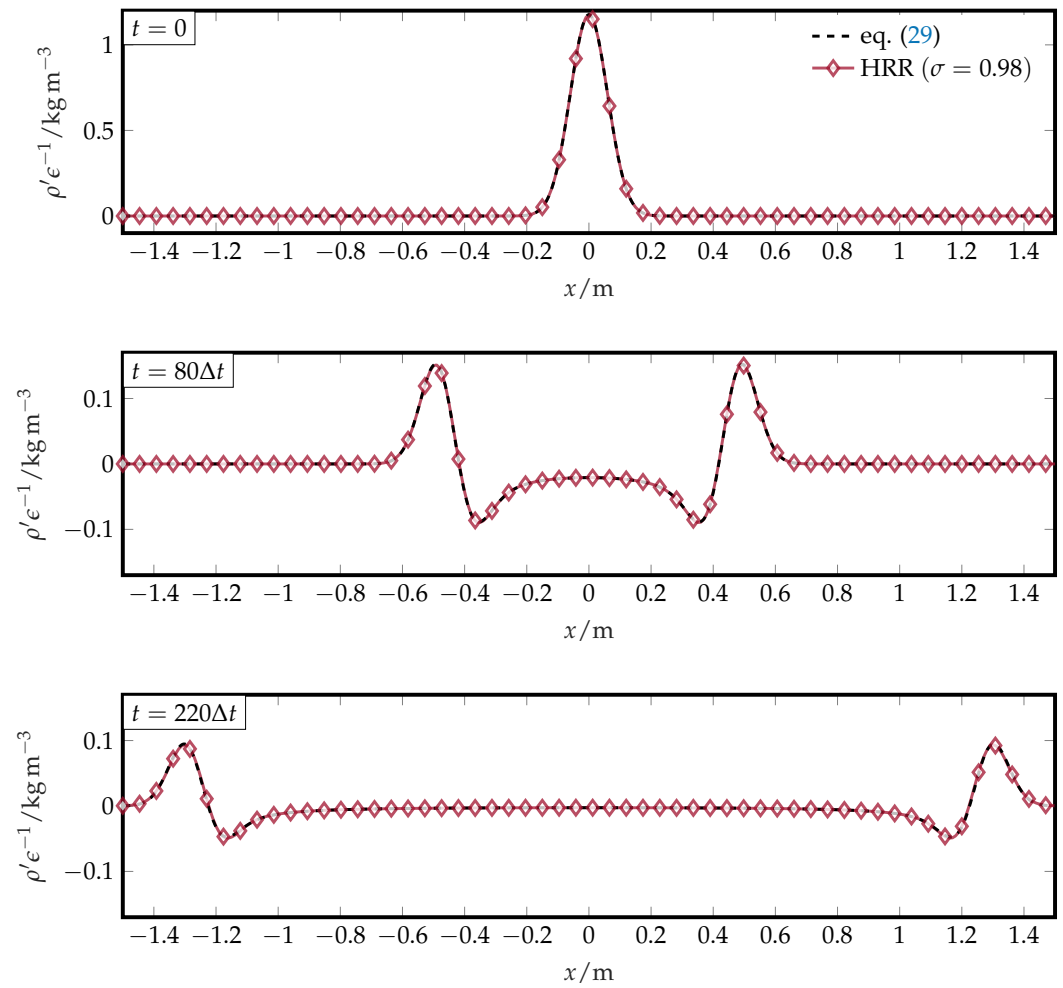


Figure 6. Temporal evolution of the acoustic pulse with HRR collision on a uniform grid compared with the analytical solution.

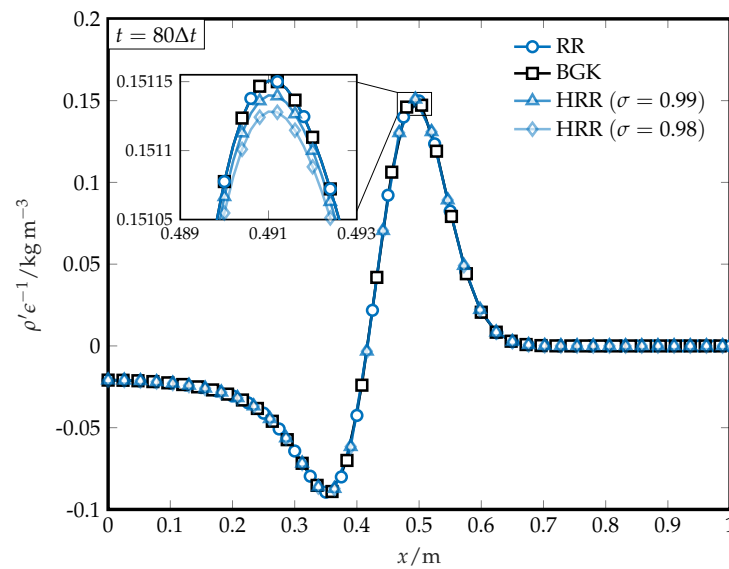


Figure 7. Effect of increased numerical dissipation of the HRR model on the pulse amplitude for a uniform grid.

Pulse reflections for different grid refinement methods are shown in Figure 8 along the abscissa, with the GTI represented by the dashed vertical line at $x = 0$. First of all, it should be noted that the excellent agreement of cc and cm schemes, including our HRR

adaptation from [5], with the uniform fine grid on the right side of the interface indicates an undisturbed passage of the pulse and validates the approach for acoustic applications.

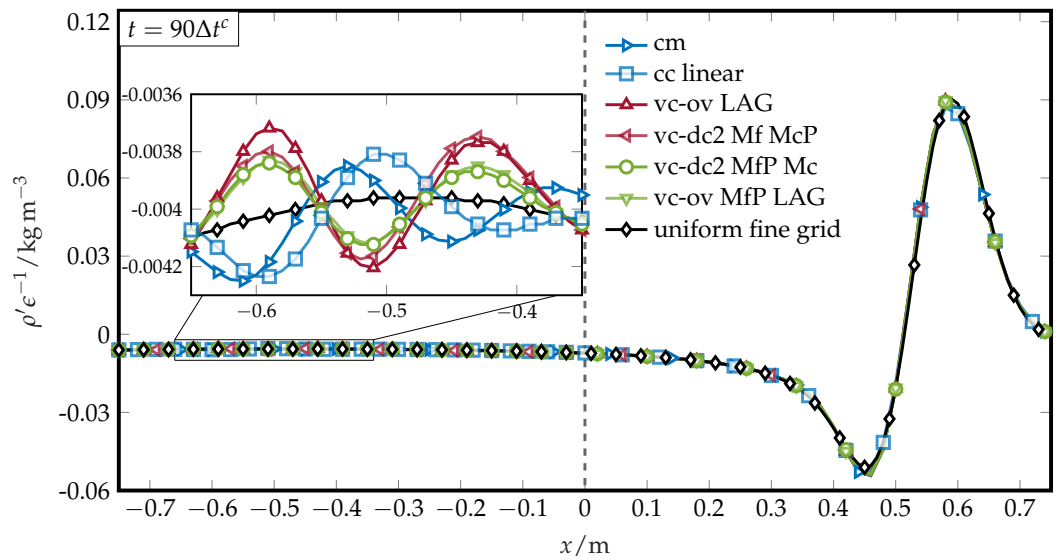


Figure 8. Spurious reflection of the acoustic pulse at the GTI for various refinement schemes and HRR collision model with $\sigma = 0.98$.

Qualitatively speaking, it can be stated that cc with linear explosion (cf. Equation (25)) cm, and vc-dc2 (cf. Equation (23)) exhibit a similar amount of reflection. The cc method with uniform explosion (cf. Equation (24)) has not shown significant differences to cc linear for this test case. In agreement with [4], the vc-ov method with the Lagrava filter produces a stronger reflection compared with vc-dc, whereby the difference to vc-ov, i.e., without stabilizing filtering, is only marginal, as can be seen in Figure A3 in the Appendix. Nevertheless, the reflection is an order of magnitude smaller compared with the pulse for all methods. The phase inversion observed in the reflected waves between cc and cm on the one side and the vc schemes on the other is possibly related to the temporal interpolation within the latter. However, no further investigation has been carried out in this context. The shift for cm is caused by the interface extending over $2\Delta x^c$ and the resulting difference in interface node arrangement.

A comparison between the two reconstruction variants for vc-dc discussed in Section 2.5 illustrates a noticeable reduction in reflection when retaining a maximum of available coarse states during grid communication, which diminishes aliasing effects and adds numerical dissipation to the scheme. This means a reconstruction of the fine distributions in \mathcal{M}^f and \mathcal{P} , so that in addition to the missing distribution functions at \odot , known states that originate from hanging nodes \otimes are also replaced utilizing information from the coarse interface node \square . Afterwards, only coarse states belonging to \mathcal{M}^c need to be reconstructed, providing all necessary states for the subsequent collision step. Figure A4 shows the corresponding diagram for vc-dc1. Although the MfP Mc procedure reduces the introduction of interpolation errors at \odot , this effect is balanced due to \mathcal{P} states being reconstructed by spatial interpolation at \otimes in contrast to vc-dc Mf McP, since we rely on an equal treatment of all fine interface nodes. A preceding investigation of the influence of different reconstructions at \otimes , independent of \odot , did not reveal any significant differences.

A significant reduction in reflection can be achieved for the vc-ov LAG method by an MfP reconstruction, whereby we have tested several variants, and this one has proven to be the most beneficial. Here, solely the known states $f_i^f, \forall i \in \mathcal{Q}^f$ are kept, while fine states in \mathcal{M}^f and \mathcal{P} are replaced with the help of the coarse partner \square . Furthermore, all coarse functions are replaced using information from the fine partner node \circ . Relying on this

form of reconstruction, the reflection amplitude is reduced to a degree similar to that of vc-dc2 MfP Mc, hence falling below the original vc-dc2 Mf McP algorithm.

To conclude this subsection, the following can be summarized for the Gaussian acoustic pulse benchmark:

- For pure acoustic scenarios, i.e., without any background flow, vc-dc2, cc and cm provide similar accuracy with regards to spurious reflections at the interface.
- A phase inversion of the reflected wave, which is possibly related to temporal interpolation, is observed between cc and cm schemes on the one side and vc schemes on the other.
- Spatial filtering applied during $f \rightarrow c$ communication in vc-ov, has no significant impact on the results.
- Partial reconstruction procedures lead to a considerable decrease of reflected pulse amplitude in the case of vc-ov LAG and a smaller, yet noticeable reduction for vc-dc1 and vc-dc2.

3.2. Convected Acoustic Wave

The convected acoustic wave test case is suitable for investigating the interaction between spurious acoustic modes and grid transitions, since in contrast to the Gaussian pulse, these modes are not static and may therefore be convected across an existing interface.

Using a vc-ov LAG grid refinement scheme Astoul et al. analyzed in [3] the energy transfer that occurs at the GTI between a spurious mode excited during initialization (termed *incident* spurious mode) and physical acoustic modes if the incident spurious mode is not properly attenuated before impinging the interface. They demonstrated that a significant amplification of the incident spurious mode is observed for BGK and RR collision models, which leads to subsequent generation of acoustic waves emerging from the GTI. With HRR, no such artifacts appear since the incident spurious mode is sufficiently damped before reaching the grid transition (cf. figures 16-C and 19-C in [3]). The subject of the present subsection is to investigate and compare these effects for various types of grid refinement methods, as, to the best of the authors' knowledge, this test case has only been examined in the above-quoted reference for one type of grid transition algorithm before.

As depicted in Figure 9, the acoustic wave is initialized in the fine grid of a pseudo-1D periodic domain of size $[L, \Delta x^c, \Delta x^c]$ with $L = 14$ m, according to

$$\begin{cases} \rho'(x, t = 0) = \rho_0 \epsilon \exp(-\beta(x - x_c)^2) & \bar{\rho} = \rho_0 \\ u'_x(x, t = 0) = c_s \epsilon \exp(-\beta(x - x_c)^2) & \bar{u}_x = -u_0, \end{cases} \quad (30)$$

passing the GTI located at $x = 0$ after being convected upstream against the background flow u_0 . All simulation parameters are summarized in Table 2.

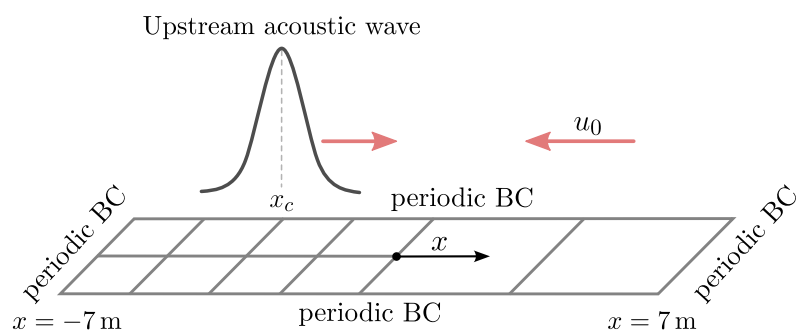


Figure 9. Schematic representation of the convected acoustic wave test case following [3].

Table 2. Parameter set for the convected acoustic wave.

$\Delta x^c/m$	$c_s/m s^{-1}$	u_0	$\rho_0/kg m^{-3}$	$\nu/m^2 s^{-1}$	ϵ	R_c/m	$(x_c/m, y_c/m)$
0.01	300	$0.1c_s$	1.17621	1.49×10^{-5}	1×10^{-4}	0.05	$(-0.1R_c, 0)$

Several distinct phenomena can be identified in this type of scenario, some of which are indicated in Figure 10 and were described in detail by Astoul et al. in [3]. As they determined by means of spectral analysis, the incident spurious acoustic mode has negative group velocity and is therefore being convected upstream towards the GTI, where it is strongly amplified. Since this numerical artifact constitutes the crucial part, we focus on it here.

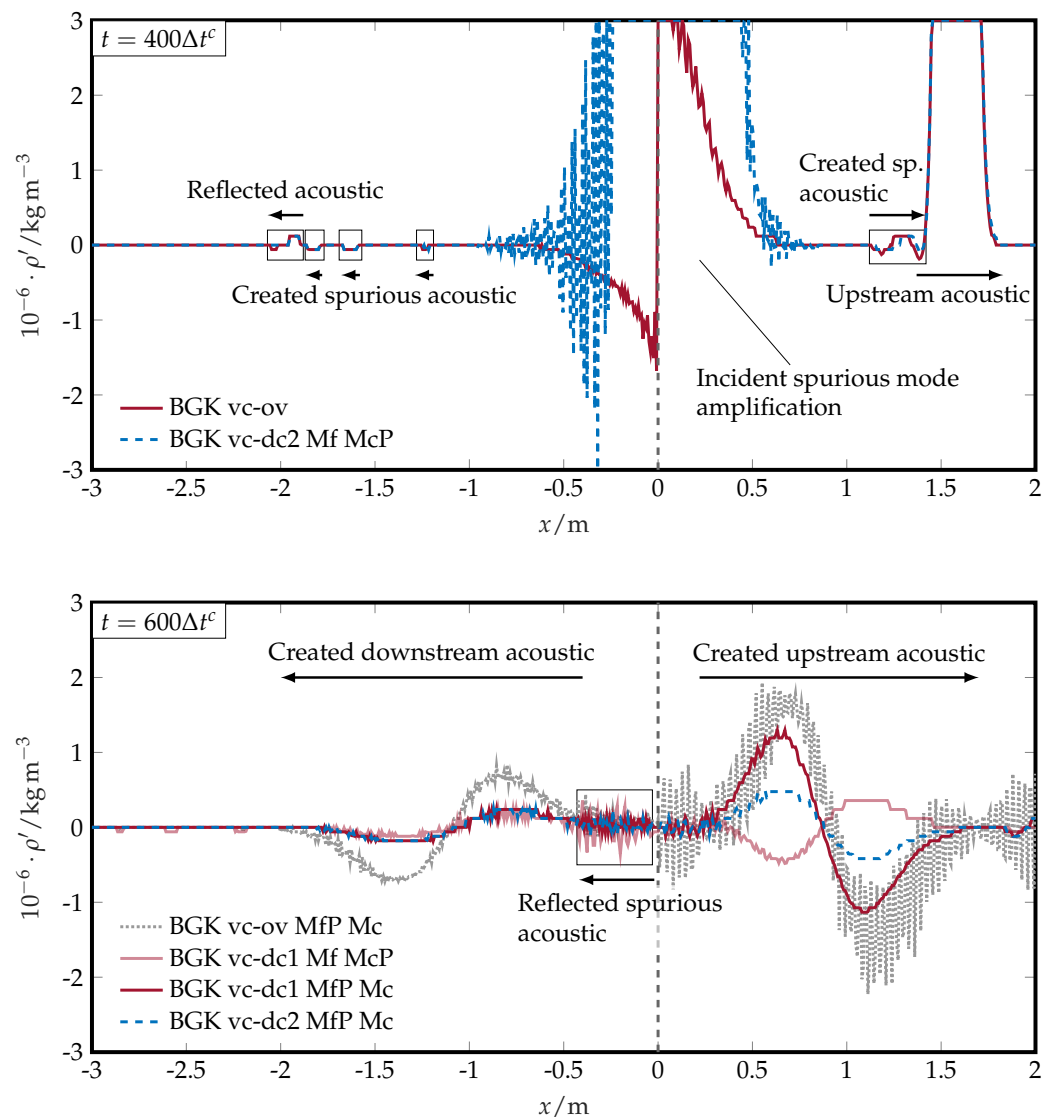


Figure 10. **Top:** Spurious mode amplification leading to instability. **Bottom:** Stabilization of vc-ov and vc-dc2 using MfP Mc reconstruction. The GTI is indicated by the dashed vertical line.

The top diagram in Figure 10 shows unbounded growth of the incident spurious mode at the GTI for BGK collision with vc-dc2, including MfP Mc reconstruction (original algorithm) and vc-ov, after the physical acoustic wave has already been convected across the grid transition, ultimately leading to instability and divergence of both simulations. Notice

that no $f \rightarrow c$ restriction is used for vc-ov. In accordance with [3], reflections and spurious acoustics generated at the GTI appear with negligible amplitude for this benchmark.

In the bottom part of the figure, the same situation is depicted with an alternative partial reconstruction procedure. When utilizing MfP Mc, i.e., retaining a maximum of known coarse states during the communication step by replacing only missing ones after reconstructing $f_i^f, \forall i \in \mathcal{M}^f \cup \mathcal{P}$, vc-dc2 is stabilized. Two acoustic waves are created at the GTI, one of which propagates upstream and the other downstream. This situation corresponds to the phenomena observed by Astoul et al. for vc-ov LAG with BGK and RR collision (cf. top of Figure 11), with the difference that the amplitudes of the created acoustics are reduced considerably when either vc-dc2 MfP Mc or vc-dc1 in its original form, i.e., including Mf McP reconstruction, is used. With MfP Mc reconstruction, vc-dc1 still exhibits a noticeable decrease in artificial acoustic wave amplitude compared with vc-ov LAG, albeit higher than vc-dc1 Mf McP. The discrepancy between the two reconstructions for vc-dc1 could be related to a mismatch in consistency for vc-dc1 MfP Mc since a maximum of fine states is employed for the iterative determination of $f_i^{(0)}$, while, on the other hand, a maximum of coarse states is retained during the reconstruction of distribution functions at the interface. Yet vc-dc1 MfP Mc still leads to a reduction in the reflection of the Gaussian pulse, as was shown in Section 3.1.

Regarding BGK vc-ov, several reconstruction strategies distributed among Figures 10 and 11 have been examined. Generally speaking, a $f \rightarrow c$ restriction operation was only necessary for vc-ov and vc-ov MfP with BGK collision to achieve a stable solution. All other approaches that rely on partial reconstruction of distribution functions on either level remained stable without such filtering. However, high-frequency oscillations emerge, especially in the coarse grid, if filtering is dispensed with and only coarse states belonging to \mathcal{M}^c are replaced. Furthermore, all partial reconstructions exhibited a less pronounced amplitude of the created upstream wave and a similar or weaker downstream wave compared with the full replacement, with the lowest amplitudes occurring for vc-ov Mf (LAG), amounting to a reduction of $\approx 47.6\%$ and $\approx 33.3\%$ relative to vc-ov LAG for the upstream and downstream wave, respectively.

Applying vc-ov together with RR collision, the results almost coincide with BGK vc-ov LAG. The regularization filters out detrimental high-frequency oscillations even without the use of a restriction operation. Nevertheless, the intensity of the artificial waves is essentially determined by the refinement method if no attenuation of the incident spurious mode is present prior to its interaction with the GTI, as it is the case with HRR.

While the cm approach leads to a similar amplitude for the created acoustics and smooths out oscillations by means of implicit filtering of f_i^{neq} during $f \rightarrow c$ communication due to trilinear spatial interpolation, the cc method demonstrates substantially different properties. With the cc algorithm, neither high-frequency oscillations nor the up- and downstream acoustic waves are generated at the GTI for BGK collision. Regardless of the order of explosion, no harmful interactions of the incident spurious mode with the grid refinement interface can be observed, resulting in a behavior akin to that produced with the HRR collision model, so that only the spurious reflection caused by the sudden resolution change as well as some created low-amplitude spurious waves remain.

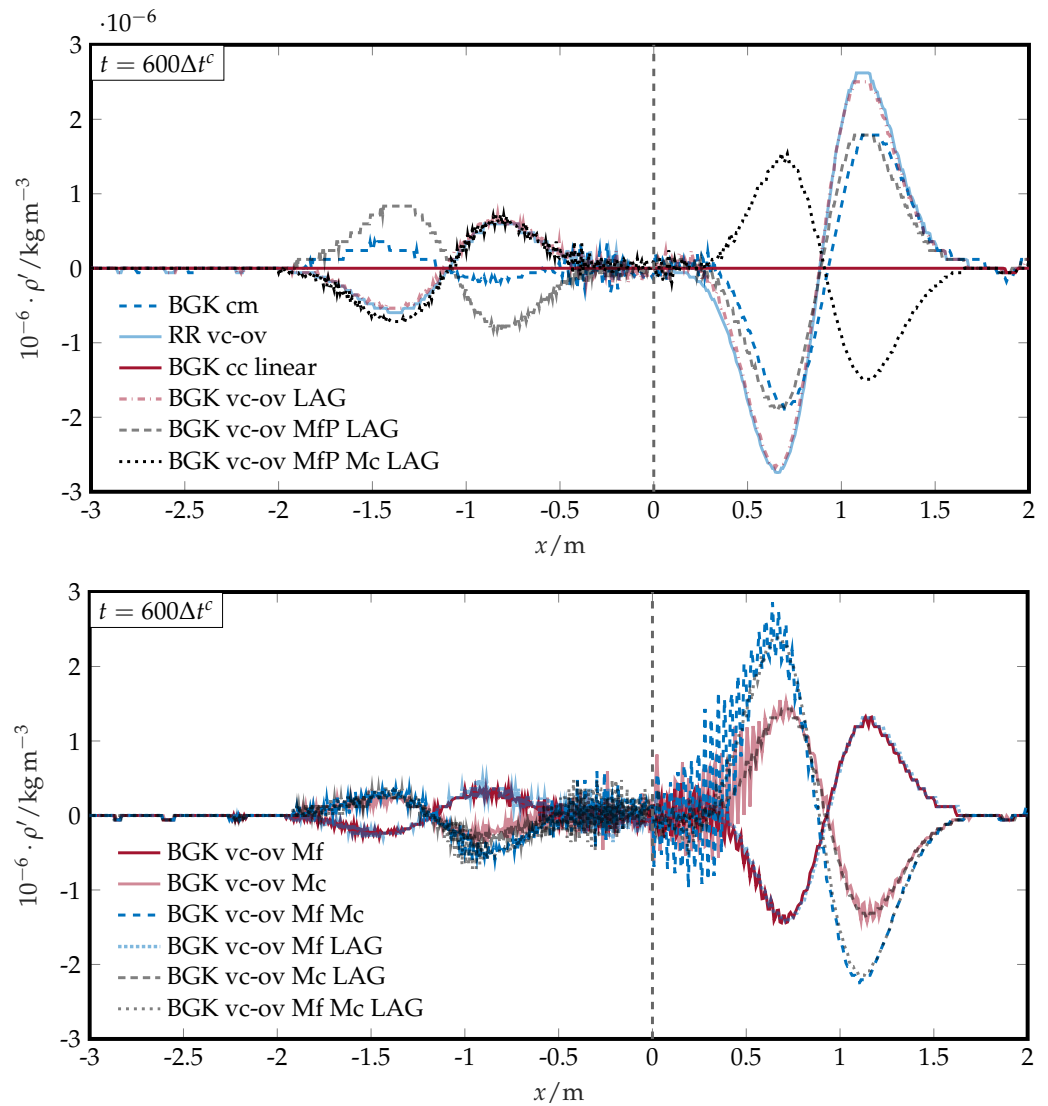


Figure 11. Spurious acoustic waves and high-frequency fluctuations emitted from the GTI with vc and cm algorithms due to detrimental interaction with non-hydrodynamic modes. No such numerical noise is present for cc linear.

Our first hypothesis was that the increased numerical dissipation of the cc method compared with vc and cm we described in our previous study [5] effectively impedes the excessive growth of the incident spurious mode at the GTI. Another explanation can be given by means of Figure A5, where the cc algorithm is depicted with first- and second-order accurate explosion and tighter ordinate scaling at $t = 600\Delta t^c$. Since no indication of the interaction between the incident spurious mode and the GTI is present up to machine epsilon, which one would not expect if numerical dissipation were responsible for its mitigation, the scheme’s inherent mass and momentum conservation properties are likely to explain the favorable performance of the cc algorithm in the context of the convected acoustic wave test case. Even though the central Equation (21) of the direct-coupling method is essentially built on the same premise [4], the required temporal and spatial interpolations within the scheme may still violate mass and momentum conservation, thereby inducing the observed behavior.

Concerning the cause of the additional dissipation of the cc scheme, we incorporated the coalescence procedure—i.e., averaging of the *complete* velocity distribution function f_i , instead of just filtering f_i^{neq} during $f \rightarrow c$ communication—into the cm algorithm to see whether this would affect the results. However, no significant changes could be

identified. This disproves the assumption we expressed in [5] and means that the root of the dissipation is not linked to coalescence but possibly to the utilization of over-advanced fine distribution functions in the collision step during asynchronous iterations, which is a known source of error of the scheme [15,67]. Further research is necessary in this regard and will be left open for future work.

To conclude this subsection, the following can be summarized for the convected acoustic wave benchmark:

- If no restriction of fine states during $f \rightarrow c$ communication is applied in vc-ov with classical BGK collision, divergence occurs due to incident spurious acoustic mode growth at the grid transition interface. Similar stability problems are encountered with BGK vc-dc2, whereas vc-dc1 remains stable.
- Relying on a partial reconstruction procedure during grid communication stabilizes both BGK vc-ov and BGK vc-dc2. Clearly visible high-frequency oscillations are encountered in case of vc-ov, superimposing the created up- and downstream spurious acoustic waves.
- Utilizing a restriction operation and/or RR collision stabilizes vc-ov, damping high-frequency oscillations, albeit showing increased amplitudes of the created up- and downstream acoustics compared with the partial reconstruction procedure. Consequently a combination of both steps is preferable with BGK collision in this case. The combined scheme leads to a behavior akin to that of stabilized vc-ov.
- The cell-centered schemes completely suppress the incident spurious mode growth and associated generation of the spurious up- and downstream acoustics, resulting in a nearly undisturbed passage of the convected physical wave across the transition. This is attributed to the scheme’s inherent mass and momentum conservation properties. Thus, for this benchmark, a similar accuracy is achieved with the BGK collision operator as with HRR collision (see [3]), when employing cc either with linear or uniform explosion.

3.3. Convected Barotropic Vortex

To investigate the effect of transporting vorticity across various types of grid refinement interfaces, we next consider the barotropic vortex that was introduced by Wissocq et al. in [51] and has since been utilized in several studies on spurious aeroacoustic emissions in lattice Boltzmann simulations on non-uniform grids [2–4].

The vortex is initialized in the fine grid of a pseudo-2D periodic box of size $[L, L, \Delta x^e]$ with $L = 10$ m, which is schematically depicted in Figure 12, by the relation

$$\begin{cases} \rho'(x, y, t = 0) = \rho_0 \left(\exp \left[\frac{\epsilon^2}{2c_s^2} \exp \left(-2\beta \left((x - x_c)^2 + (y - y_c)^2 \right) \right) \right] - 1 \right) & \bar{\rho} = \rho_0 \\ u'_x(x, y, t = 0) = -\epsilon \sqrt{2\beta} (y - y_c) \exp \left(-\beta \left((x - x_c)^2 + (y - y_c)^2 \right) \right) & \bar{u}_x = u_0 \\ u'_y(x, y, t = 0) = \epsilon \sqrt{2\beta} (x - x_c) \exp \left(-\beta \left((x - x_c)^2 + (y - y_c)^2 \right) \right) & \bar{u}_y = 0 \end{cases} \quad (31)$$

and convected across the GTI located in the middle of the domain. A summary of all relevant simulation parameters is provided in Table 3.

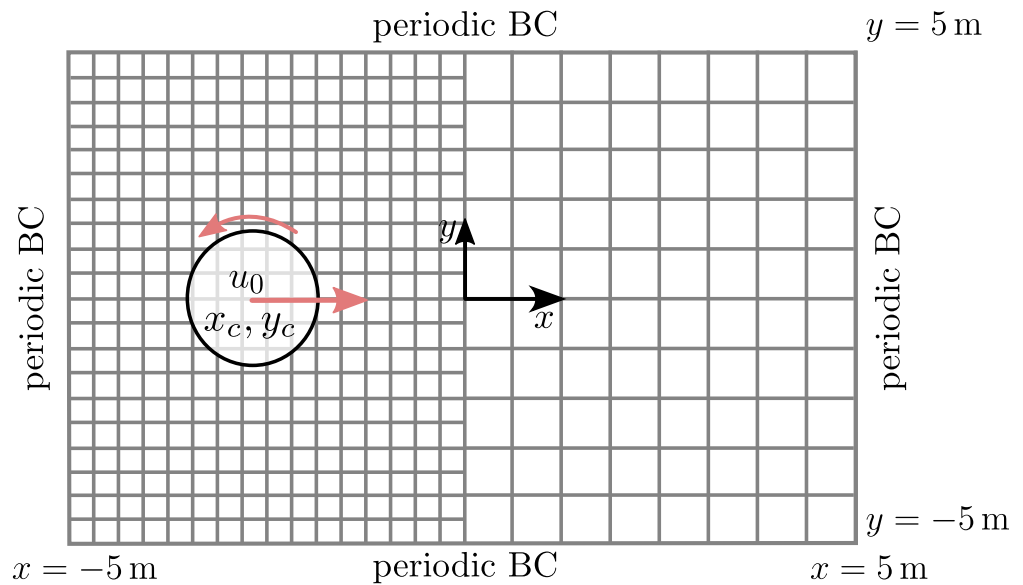


Figure 12. Schematic representation of the calculation domain for the convected barotropic vortex test case following [3].

Table 3. Parameter set for the convected barotropic vortex.

$\Delta x^c / \text{m}$	$c_s / \text{m s}^{-1}$	u_0	ϵ	$\rho_0 / \text{kg m}^{-3}$	$\nu / \text{m}^2 \text{s}^{-1}$	R_c / m	$(x_c / \text{m}, y_c / \text{m})$
0.02	300	$0.1c_s$	$0.15c_s$	1.17621	1.49×10^{-5}	0.06	$(-6R_c, 0)$

As can be verified directly from Equation (31), the vortex is characterized by a perturbation in both the velocity and density field, thereby exciting spurious shear and acoustic modes with a severely negative impact on stability and accuracy in the case of locally refined grids. Similar to the convected acoustic wave test case in Section 3.2, harmful interactions with the grid transition can lead to spurious mode amplification and subsequent contamination of the flow field if these modes are not properly attenuated before reaching the interface. Such a situation is illustrated in Figure 13. The RR collision operator does not filter out all spurious modes excited during initialization and is thus characterized by a greater amount of artificial noise produced for vc-ov LAG compared with the HRR model [3] with the same refinement algorithm and a hybridization factor of $\sigma = 0.98$, i.e., two percent of strain-rate tensor reconstruction by means of central finite differences.

Contrary to this, with cc-linear, the divergence fields for RR and HRR appear identical, apart from the clearly visible spurious modes for RR. Here, we again employ our HRR adaptation for the cc algorithm introduced in [5]. The vortex crosses the interface with a significantly less pronounced deformation relative to vc-ov LAG, attributed to the inherent mass and momentum conservation properties of the cc scheme. Figure A6, displaying the vorticity field, confirms similar observations for the spurious shear mode. All previously described results also hold true for the cell-centered algorithm with uniform explosion.

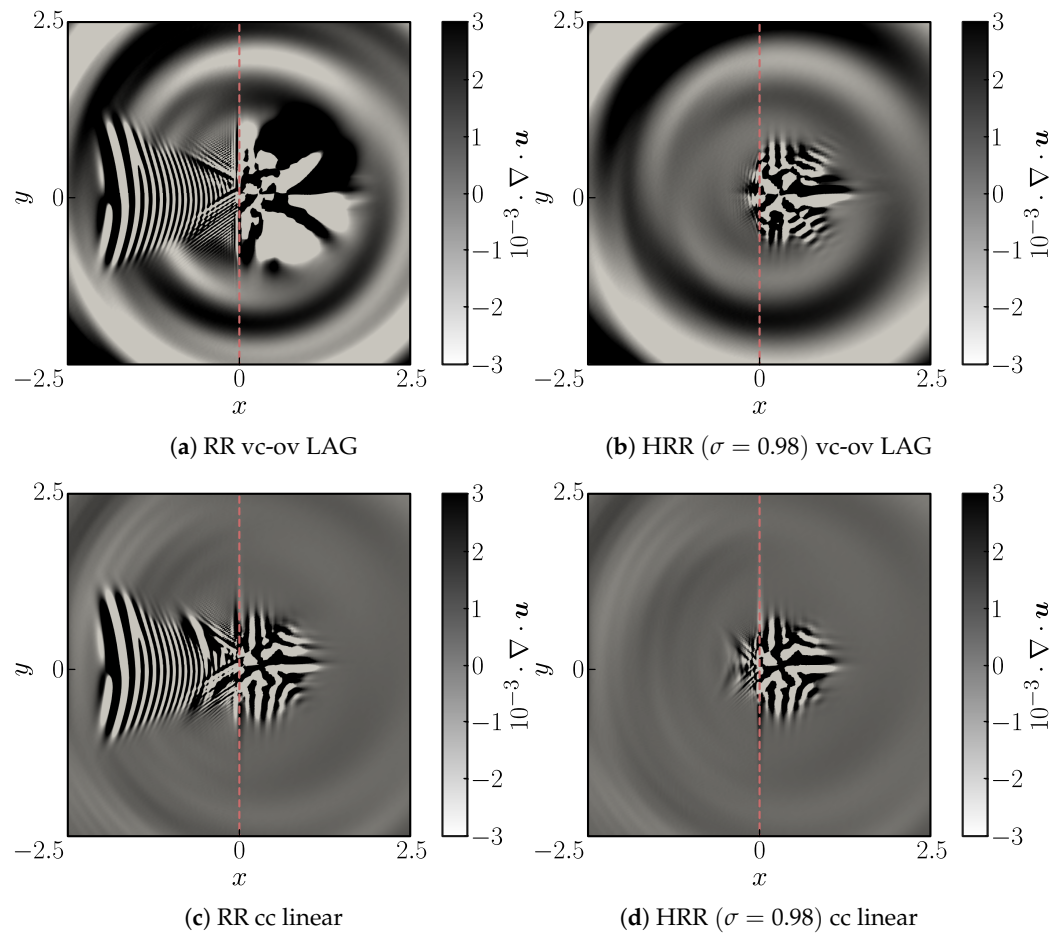


Figure 13. Top: Spurious acoustic mode amplification at the GTI resulting in additional artificial noise for RR compared with HRR with vc-ov LAG at $t = 600\Delta t^c$. **Bottom:** No such phenomena appear with the cell-centered algorithm. Units: $[x] = \text{m}$, $[y] = \text{m}$, $[\nabla \cdot \mathbf{u}] = \text{s}^{-1}$.

For the remaining analysis, we rely on HRR collision to get rid of spurious mode contributions and hence extract the sole effect of the various refinement schemes with their individual interpolations and population reconstruction approaches. Figures 14 and 15 show the relative pressure field $p - p_{\text{ref}}$, with p_{ref} denoting the reference solution that has been obtained on a uniform fine grid. Since a single vortex in a homogeneous flow is not expected to emit any acoustic waves, all the appearing disturbances are of a parasitic nature with roots in the grid refinement algorithm itself [4].

The negative influence of an additional LAG or TOU restriction of fine non-equilibrium distributions during $f \rightarrow c$ communication is clearly recognizable compared with vc-ov without a filter. The highest intensity in parasitic noise in both the mean and maximum value is obtained with the cm algorithm that combines an equivalent filtering of non-equilibria by utilization of trilinear interpolation with an increased spatial decoupling of the fine and coarse interface nodes, since an overlap width of at least two coarse cells is necessary. Accordingly, enlarging the distance between interface nodes to an overlap size of two (vc-ov2) and three (vc-ov3) is accompanied by a gradual increase in the emitted noise for the vc-ov algorithm.

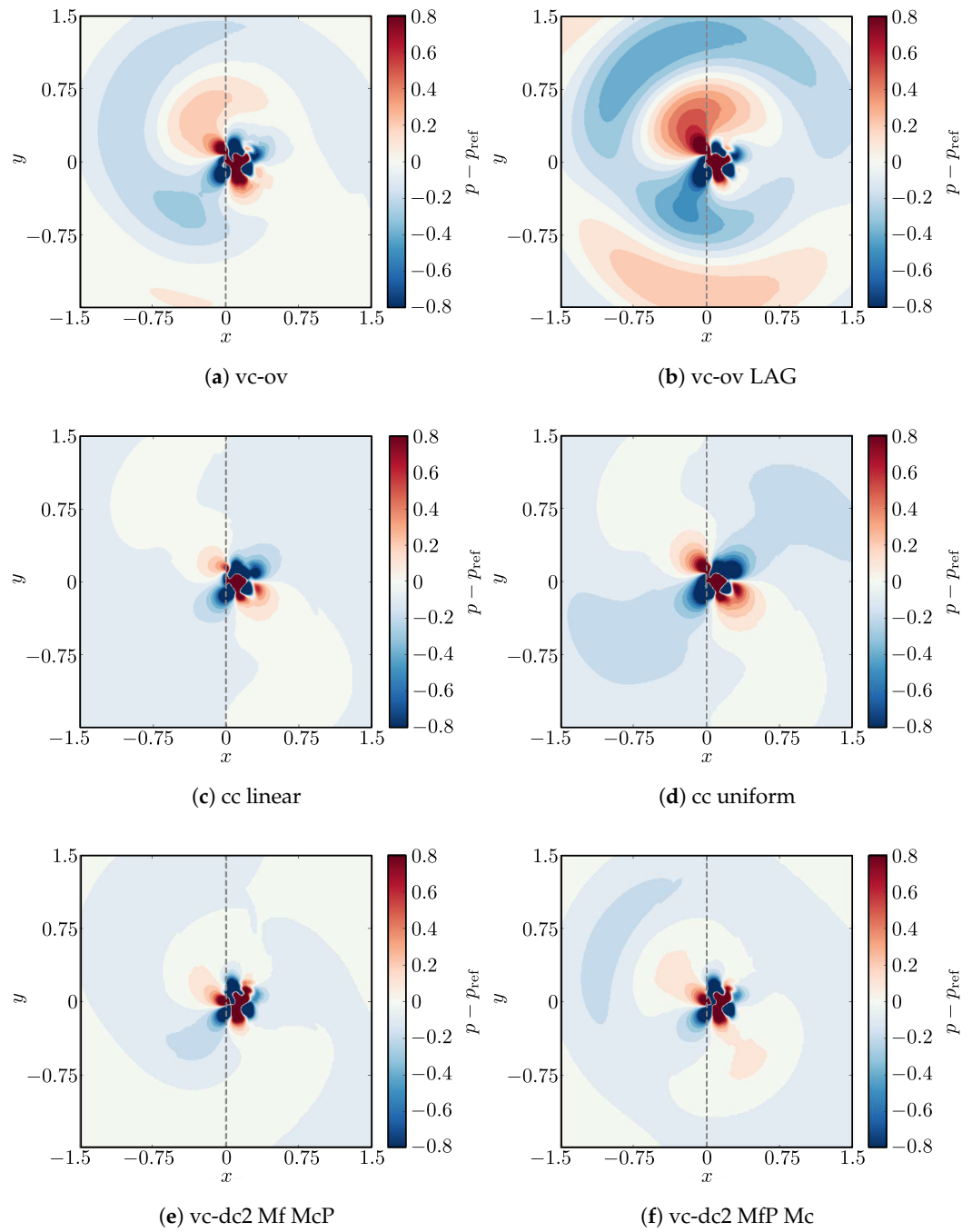


Figure 14. Relative pressure $p - p_{\text{ref}}$ contours of the convected barotropic vortex as it passes through the GTI for various refinement schemes at $t = 400\Delta t^c$. The GTI is indicated by the dashed vertical line at $x = 0$. All simulations have been carried out with the HRR collision model ($\sigma = 0.98$). Units: $[x] = \text{m}$, $[y] = \text{m}$, $[p - p_{\text{ref}}] = \text{Pa}$.

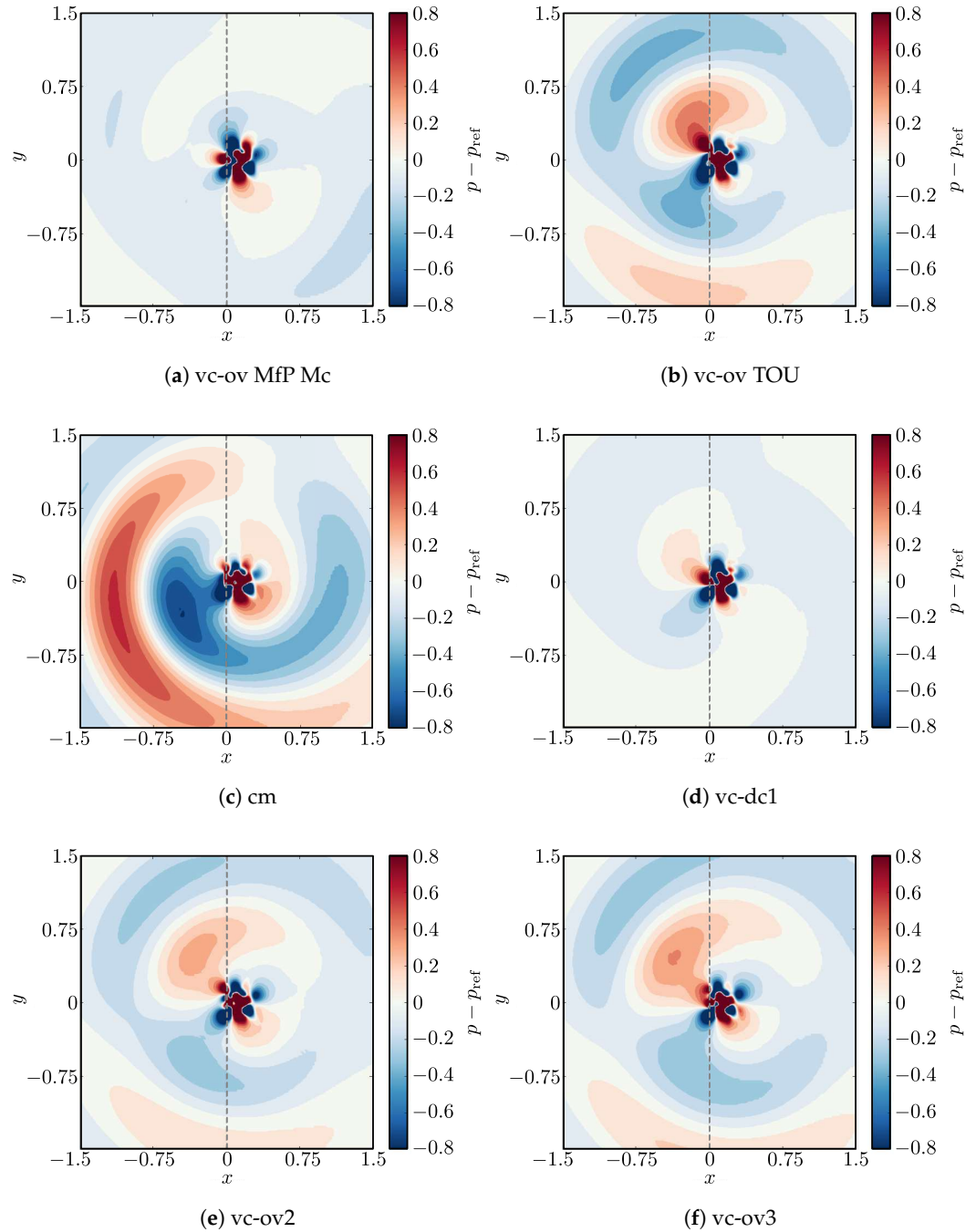


Figure 15. Relative pressure $p - p_{\text{ref}}$ contours of the convected barotropic vortex as it passes through the GTI at $t = 400\Delta t^c$. Units: $[x] = \text{m}$, $[y] = \text{m}$, $[p - p_{\text{ref}}] = \text{Pa}$.

In accordance with the observations described for the preceding test cases, the cell-centered and vertex-centered direct-coupling schemes qualitatively produce the least disturbed pressure fields. Furthermore, a substantial improvement with regards to the emission of parasitic noise is obtained in the case of the vc-ov algorithm with a partial MfP Mc reconstruction, meaning retaining a maximum of available coarse information by replacing only missing coarse functions as well as fine functions belonging to the \mathcal{P} and \mathcal{M}^f subsets. For a more precise delimitation of the perceptible differences between the various schemes, 32 pressure probes have been placed equidistantly in the far field of the vortex at a radial distance of 2 m relative to the center. Data are collected at these probes until $t = 700\Delta t^c$ to produce directivity maps together with azimuthally averaged and maximum values of

the Overall Sound Pressure Level defined as $OASPL = 20 \log_{10}(\hat{p}/p_0)$ with RMS pressure \hat{p} and a reference value of $p_0 = 20 \mu\text{Pa}$. The corresponding results are shown in Figure 16. Recalling that an increase of the sound pressure level by 3 dB is equivalent to doubling the sound pressure [31], the strong attenuation of the parasitic noise with vc-ov MfP Mc becomes evident. By relying on partial population reconstruction, we are able to reduce the mean OASPL by 3.93 dB and the peak value by 4.2 dB, with the emission pattern being altered mainly in the fine grid and along a direction parallel to the interface. The algorithm of Lagrava results in a deterioration of 6.5 dB and 6.05 dB relative to vc-ov in the mean and maximum value, respectively, whereby the parasitic emission can be marginally decreased with the anisotropic Touil filter.

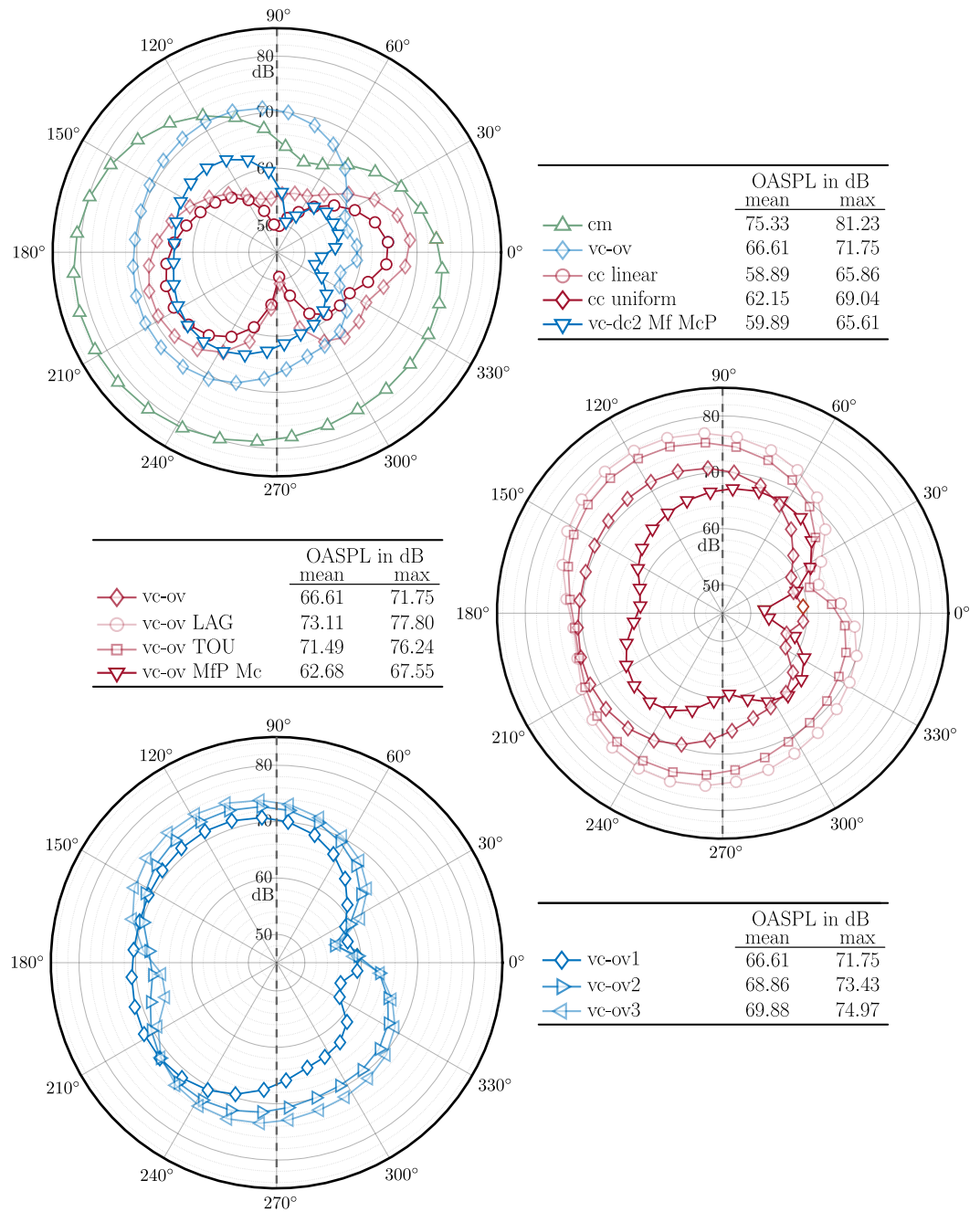


Figure 16. Directivity maps and corresponding mean and maximum values of OASPL of spurious pressure waves for the convected barotropic vortex measured in the far field following [4]. All simulations have been carried out with the HRR collision model ($\sigma = 0.98$). The GTI is indicated by the dashed vertical line.

As for the cc scheme, the linear interpolation of coarse post-collision states achieves a significant improvement of 3.26 dB and 3.18 dB in the mean and maximum OASPL, respectively, compared with uniform explosion and the lowest average sound level of all analyzed refinement algorithms. In the maximum value, only vc-dc2 in its original Mf McP reconstruction form produces less artificial noise, being 0.25 dB below cc linear. Our partial reconstruction alternative of vc-dc2 Mf Mc turns out to be slightly worse than the original form with $OASPL_{\text{mean}} = 61.58$ dB and $OASPL_{\text{max}} = 66.81$ dB, but still performs better than cc uniform.

To conclude this subsection, the following can be summarized for the barotropic convected vortex benchmark:

- If the HRR collision operator is employed to filter out non-hydrodynamic modes, cc linear and vc-dc2 Mf McP demonstrate the most advantageous properties in terms of suppressing spurious artifacts.
- In the case of the RR collision operator, cell-centered approaches are found to be the only schemes examined in this study that are able to prevent disturbances identified with harmful interactions between spurious shear and acoustic modes convected across the grid transition and the refinement interface.
- Use of a restriction operation during $f \rightarrow c$ communication has a negative impact on the spurious noise emission of vc-ov, whereby an anisotropic Touil filter performs slightly better than the arithmetic averaging of Lagrava.
- The emission characteristics of the vc-ov algorithm can be significantly improved by partial reconstruction and shifted towards the range of cc uniform.

3.4. Three-Dimensional Jet Flow

To conclude this work, we consider a three-dimensional jet test case, which represents a particular challenge for a grid refinement scheme. As schematically depicted in Figure 17, the jet enters the calculation domain of size $[L_x = 2.6 \text{ m}, L_y = 1.8 \text{ m}, L_z = 1.8 \text{ m}]$ into the fine grid through an orifice and orthogonally impinges the grid transition at a high Reynolds number of $Re = u_0 d / \nu \approx 1 \times 10^6$. To ensure a stable solution under these demanding conditions, we utilize the HRR collision model with the hybridization parameter set to $\sigma = 0.98$.

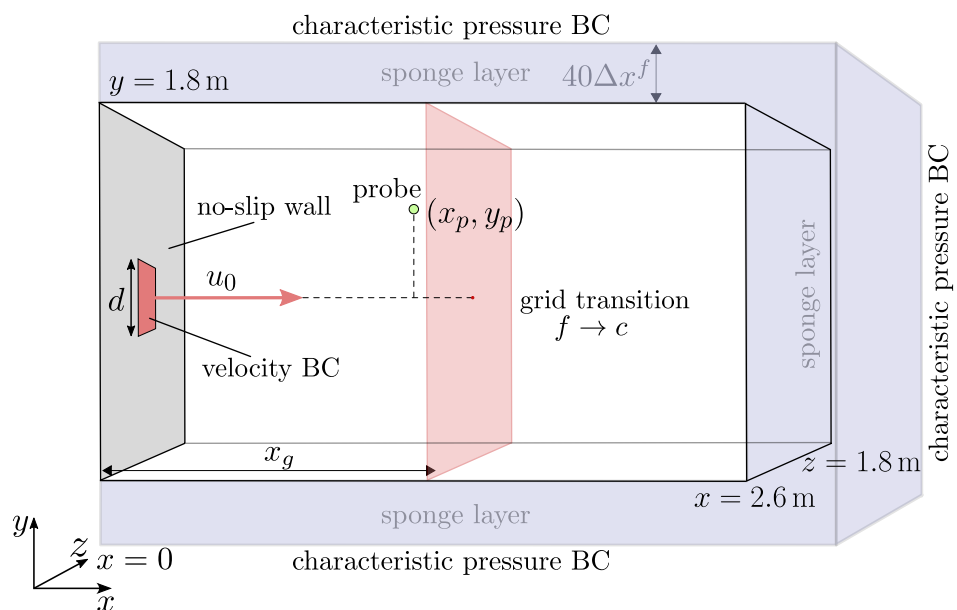


Figure 17. Schematic representation of the calculation domain for the 3D jet flow test case.

In order to prevent pressure wave reflections at the lateral boundaries and the outflow, we employ a combination of sponge layers with linearly increasing viscosity as well as the characteristic pressure conditions described in Section 2.4 and set the relaxation constant for the entering wave amplitude to $K_1 = 1 \times 10^{-3}$. A summary of all other relevant simulation parameters is provided in Table 4.

Table 4. Parameter set for the jet flow.

$\Delta x^c/m$	Ma	$u_0/m\ s^{-1}$	$\rho_0/kg\ m^{-3}$	$\nu/m^2\ s^{-1}$	d/m	x_g/m	$(x_p/m, y_p/m)$
0.01	0.1	80	1.225	1.39×10^{-5}	0.18	1.0	(0.8, 0.6)

The inflow boundary is separated from the surrounding characteristic pressure boundaries by a simple bounce-back no-slip condition to avoid instability. We understand that reflections from this wall will alter the results in absolute terms. However, since we are interested exclusively in a comparison of the individual refinement variants and use this setup in the same form for all methods, this is a systematic error that does not significantly affect the acquired findings.

Qualitative results are given in Figure 18, representing the time instant at $t = 4000\Delta t^c$ when the jet just barely passed through the grid transition with the frontmost part. The jet itself is visualized by means of contours of the Q -criterion with $Q = 5 \times 10^5$, colored by velocity magnitude. In the background, parasitic noise is displayed as disturbances in the velocity divergence field.

First of all, it can be stated that the jet tip is structurally influenced only to a minor extent by the presence of the interface and thus appears similar for all schemes. Compared with the reference solution obtained on a uniform fine grid, high-intensity spurious waves are generated at the GTI and spread radially outward for the three depicted vc-ov variations and the cm algorithm. The difference in the shape of the disturbances emerging for cm compared with vc-ov is likely caused by the spatial separation of interface nodes extending over a width of two coarse cells in the former scheme. In accordance with the convected acoustic wave and convected barotropic vortex test cases, an increase in spurious noise is noticed with the LAG restriction for vc-ov, although not as pronounced as in the aforementioned benchmarks. Moreover, relying on a partial MfP Mc reconstruction, a noticeable reduction in the spurious wave intensity is achieved. With this reconstruction procedure, all available and valid coarse post-streaming distribution functions are retained instead of being reconstructed using information from the fine grid. This adds dissipation to the scheme and mitigates aliasing errors since the amount of scales not resolvable on the coarse grid is decreased. However, the spurious source remains clearly visible for vc-ov MfP Mc.

Again, the cell-centered and vertex-centered direct-coupling schemes prove to exhibit the most favorable properties in terms of aeroacoustics of all investigated schemes. For uniform explosion as well as vc-dc1 no significant differences have been identified to the cc linear and vc-dc2, respectively. Despite some remaining artifacts, such as high-frequency oscillations appearing in the fine grid, no high-intensity spurious wave source is present for either of these methods.

Quantitative results are summarized in Figure 19 in terms of Power Spectral Density (PSD) estimates \hat{S}_p of pressure fluctuations evaluated at the probe position marked in Figure 17. From the moment the jet impinged the transition, time series data have been collected over a period of 0.1 s, corresponding to approximately 1.4×10^4 samples. In order to mitigate frequency leakage, we partitioned the data into eight segments with 50% overlap and applied the flattop window function before calculating the PSD by means of Welch's method. As a reference, the uniform fine grid solution is once again included.

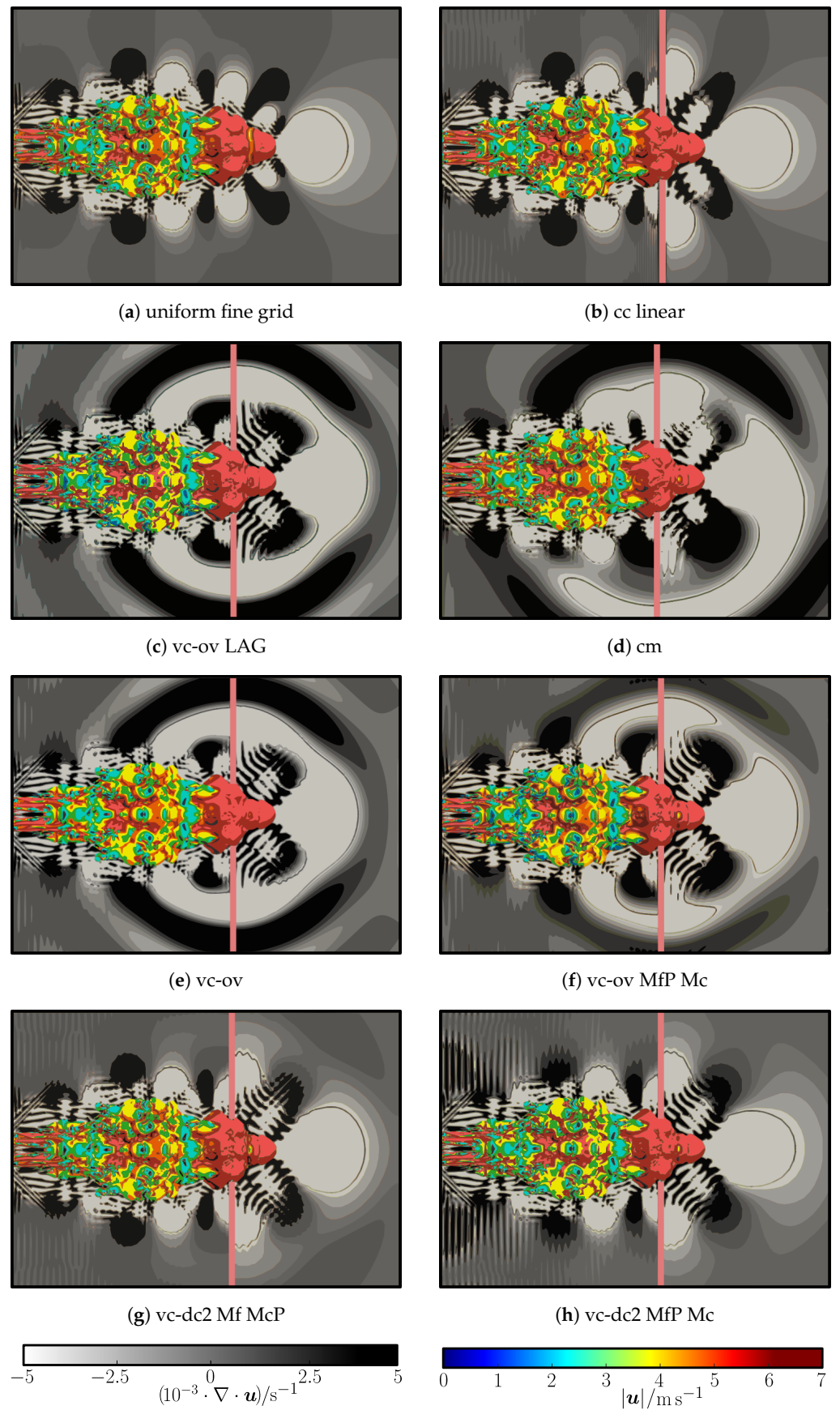


Figure 18. Spurious noise caused by the jet passing through the GTI after $t = 4000\Delta t^c$. The jet is visualized using Q -contours with $Q = 5 \times 10^5$ colored by velocity magnitude. The GTI is indicated by the red vertical line.

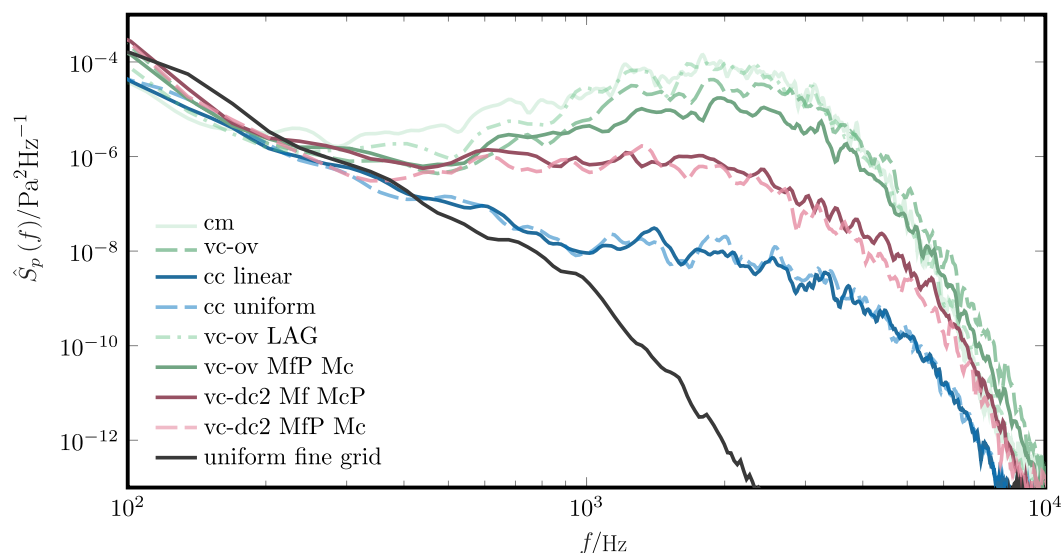


Figure 19. PSD of pressure fluctuations at the probe position for various grid refinement algorithms.

The major qualitative differences previously described are clearly reflected between the individual methods in the mid-to-high frequency range, where three distinct groups can be identified, separated by approximately one to two orders of PSD magnitude. The first one consisting of the cm scheme as well as the vc-ov methods, with the influences of filtering and partial reconstruction described above being evident. The second group is formed by the vc-dc methods, which demonstrate a significant improvement in PSD. A slight downward shift can be seen with vc-dc2 MfP Mc compared with Mf McP, despite the obvious high-frequency perturbations in the fine grid in Figure 18.

Notwithstanding the similar qualitative results, there is another substantial leap to the third and final group, the cc schemes, which in turn show no recognizable differences between one another and prove the most suitable in the case of the jet. Although it remains to be emphasized that none of the methods can be completely free of artificial noise, this test once again highlights the essential importance of the cc scheme's inherent mass and momentum conservation properties for the mitigation of grid-induced noise.

To conclude this subsection, the following can be summarized for the three-dimensional jet benchmark:

- In accordance with observations obtained in the previous benchmark simulations, cell-centered schemes show the most favorable properties in terms of grid-induced noise, exhibiting a substantial leap in PSD spectra over the mid- to high-frequency range compared with all other investigated methods for the jet flow.
- For vertex-centered methods, a significant improvement is achieved by the direct-coupling approach.

4. Summary and Outlook

In this study, established hierarchical grid refinement techniques for the lattice Boltzmann method have been examined in the context of spurious aeroacoustic emissions. Particular attention was devoted to a juxtaposition of different classes of grid structures comprising vertex-centered (vc), cell-centered (cc), and combined methods (cm), since a corresponding quantitative analysis has been lacking in the literature to date. Furthermore, various existing variations of vertex-centered and cell-centered methods were included in the study.

With regards to vertex-centered methods, the widespread algorithm of Lagrava served as a foundation (vc-ov LAG). We analyzed the effects of a more sophisticated anisotropic filter during fine-to-coarse communication proposed by Touil et al. (vc-ov TOU) and of

omitting the restriction operation entirely (vc-ov). A more recent vertex-centered direct-coupling algorithm (vc-dc) was considered that dispenses with a grid overlap and has been proven to exhibit favorable characteristics for aeroacoustics due to improved conservation properties. For both the vc-ov and vc-dc schemes, alternative formulations differing in the particle sets to be reconstructed at interface nodes have been studied.

Concerning cell-centered approaches, uniform explosion as well as linear interpolation of coarse post-streaming functions during the explode procedure were looked at. In addition to the classical Bhatnagar–Gross–Krook (BGK) collision operator, we also considered the more advanced recursive regularized (RR) and hybrid-recursive regularized (HRR) collision models to be able to distinguish between multiple sources of parasitic noise. Within the HRR model, the hybridization parameter that determines the proportion of strain-rate tensor reconstruction by means of finite differences was set to $\sigma = 0.98$ in all cases, since this value is recommended in the literature for industrially relevant flow scenarios.

Four test cases with increasing complexity and significance for aeroacoustic applications have been investigated, the first of which comprised a Gaussian acoustic pulse in Section 3.1 that spread across a grid transition interface (GTI). An alteration in numerical properties between the coarse and fine grid due to the sudden resolution change as well as interpolations utilized in the individual refinement methods inevitably causes a spurious reflection of the pulse. In this purely acoustic scenario, the most pronounced reflection amplitude—albeit still being very small relative to the physical pulse—was present for vc-ov, independent of whether a restriction operation was included, while no significant differences have been identified between the cc and vc-dc schemes. Through an alternative reconstruction approach during the grid communication step based on retaining as much information from the coarse interface node as possible, we were able to achieve a noticeable reduction in the pulse amplitude for vc-dc1 and vc-dc2. Referring to the nomenclature introduced in Section 2.5, this MfP Mc termed variant first reconstructs fine distribution functions belonging to subsets \mathcal{M}^f and \mathcal{P} and afterwards only missing coarse functions in \mathcal{M}^c , in contrast to the original vc-dc formulation, where a Mf McP reconstruction is employed. Moreover, among many tested variations, a partial MfP reconstruction strategy displayed the strongest attenuation of the pulse reflection for the vc-ov LAG algorithm. In this variation, all coarse states are replaced, and valid available post-streaming states are kept. The agreement of the physical pulse with the reference solution for a uniform fine grid shows that the HRR adaptation for cc and cm is applicable for acoustics.

The second test case consisted of a convected acoustic wave. In accordance with the literature, an incident spurious acoustic mode is excited that is amplified at the GTI. With the BGK collision model, severe instabilities arise for vc-ov and vc-dc2 due to this process, which can be dealt with in several ways. Using our proposed MfP Mc reconstruction approach leads to a mitigation of the incident spurious mode amplification, thereby rendering a stable solution. For vc-ov, several partial reconstruction methods achieved a similar effect. Albeit a subsequent generation of up- and downstream acoustic waves was noticed that have been described in the literature before for vc-ov LAG, the amplitudes of these waves have been reduced considerably compared with the Lagrivas algorithm.

The cell-centered methods not only provided a stable solution with BGK, but, besides very-low-amplitude spurious waves, together with the unavoidable reflection of the physical wave, did not generate any of the previously described acoustic waves at the interface. Since no indication of these parasitic phenomena has been found up to machine epsilon, it was concluded that the inherent mass and momentum conservation properties of the cc methods are responsible for this observation.

In the convected barotropic vortex test case, the transport of vorticity across the GTI was investigated qualitatively and quantitatively. The analysis was conducted in two steps.

First, the effect of spurious mode amplification at the GTI was examined by comparison between RR and HRR collision for vc-ov LAG and cc linear. With the HRR collision operator, spurious modes are effectively dampened before reaching the GTI, thus the observed parasitic noise is solely rooted in the refinement algorithm itself. For the vc-ov LAG algorithm, significant differences appeared between RR and HRR in the vorticity and divergence fields, indicating the effect of spurious shear and acoustic modes. Similar to the convected acoustic wave test case, the cell-centered method showed no sign of such artifacts. Even though spurious modes were clearly present, no interaction with the GTI took place.

In the second step, we relied on the HRR operator to filter out detrimental non-hydrodynamic modes in order to isolate the influence of the various refinement algorithms. For cc and cm schemes, again our adaptation has been utilized. Pressure probes were placed in the far field of the vortex in order to measure Overall Sound Pressure Levels (OASPL) of the parasitic noise and provide corresponding directivity maps. A significant reduction in the azimuthally averaged and maximum OASPL of 3.9 dB and 4.2 dB, respectively, was found with a partial MfP Mc reconstruction for vc-ov compared with a full replacement of interface distribution functions. The cell-centered scheme with linear explosion showed an improvement of 3.26 dB and 3.18 dB in the mean and maximum OASPL, respectively, relative to the version including uniform explosion, and performed very similarly to vc-dc2 Mf McP (original form), being slightly better in the mean but worse in the maximum value by 0.25 dB. Our vc-dc2 MfP Mc alternative exhibited OASPL levels in between vc-dc2 Mf McP, cc linear, and cc uniform.

To conclude this paper, a high-energy jet flow impinging a planar, vertical GTI at a Reynolds number of $Re = 1 \times 10^6$ was simulated. In order to guarantee a stable solution, this test was performed using the HRR collision model. Even though a partial MfP Mc reconstruction was able to recognizably weaken the emerging parasitic sound wave for vc-ov, its intensity remained comparatively high. Out of all methods, again the cell-centered and vertex-centered direct-coupling algorithms generated the least amount of spurious noise. Despite their similar qualitative results, Power Spectral Density (PSD) estimates revealed an offset of approximately two orders of PSD magnitude in favor of the cc schemes, which conversely demonstrated no significant differences among each other.

The insights gained in this work highlight the importance of mass and momentum conservation at grid transition interfaces for the reduction in spurious emissions in aeroacoustic simulations with the lattice Boltzmann method and provide a reference for the selection of suitable refinement algorithms in this context. Despite the vertex-centered direct-coupling algorithms being built on this premise, spatial and temporal interpolations may still alter its conservation properties and explain the differences observed relative to inherently conservative cell-centered schemes.

In this study, we focused on planar, vertical grid transitions. However, inclined, stepped interfaces can exhibit deteriorating effects in vc methods due to the involved spatial interpolations at hanging nodes. Recently, Berezin et al. [68] proposed a new grid refinement method based on conversions between LBM stencils for BGK collision to provide a recalibration of populations and hence an interpolation-free algorithm. Although the barotropic vortex is part of the validation, no detailed analysis with regards to spurious emissions is given. An evaluation of this algorithm's performance in relation to the research subject presented here, together with an in-depth study including inclined grid transitions, will be left open for future work.

Author Contributions: Conceptualization, methodology, formal analysis, A.S. (Alexander Schukmann) and A.S. (Andreas Schneider); writing—original draft preparation, A.S. (Alexander Schukmann); visualization, A.S. (Alexander Schukmann) and V.H.; writing—review and editing, A.S. (Alexander Schukmann) and A.S. (Andreas Schneider); investigation and validation, A.S. (Alexander Schukmann) and V.H.; data curation, A.S. (Alexander Schukmann) and V.H.; supervision, project administration, A.S. (Andreas Schneider). All authors have read and agreed to the published version of the manuscript.

Funding: We acknowledge support by the Open Access Publication Fund of the Offenburg University of Applied Sciences.

Institutional Review Board Statement: Not applicable.

Informed Consent Statement: Not applicable.

Data Availability Statement: Data can be provided by the authors upon request.

Acknowledgments: All simulations in this study were carried out on the high-performance cluster Elwetritsch of the University of Kaiserslautern-Landau, which is part of the Alliance for High Performance Computing Rheinland-Pfalz (AHRP). We kindly acknowledge the support of the computing center. Furthermore, we would like to thank Christophe Coreixas and Thomas Astoul for fruitful discussions.

Conflicts of Interest: The authors declare no conflicts of interest.

Abbreviations

The following abbreviations are used in this manuscript:

CFD	Computational fluid dynamics
CAA	Computational aeroacoustics
GTI	Grid transition interface
LBM	Lattice Boltzmann method
LBE	Lattice Boltzmann equation
BGK	Bhatnagar–Gross–Krook (collision operator)
RR	Recursive regularized
HRR	Hybrid-recursive regularized
FD	Finite difference
PR	Projection(-based)
LODI	Local one-dimensional inviscid (equations)
CBC	Characteristic boundary condition
OASPL	Overall sound pressure level
PSD	Power spectral density
vc	Vertex-centered
cc	Cell-centered
cm	Combined
ov	Overlap
dc	Direct-coupling

Appendix A

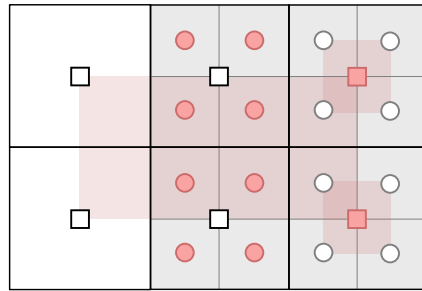


Figure A1. Cell-centered layout utilized e.g., in [64]: Since the validity ranges of the bubble functions overlap, states at coarse interface nodes \blacksquare need to be reconstructed prior to fine states at \bullet in order to provide valid information during spatial interpolation. (Remember: \circ : regular fine node, \square : regular coarse node).

Appendix B

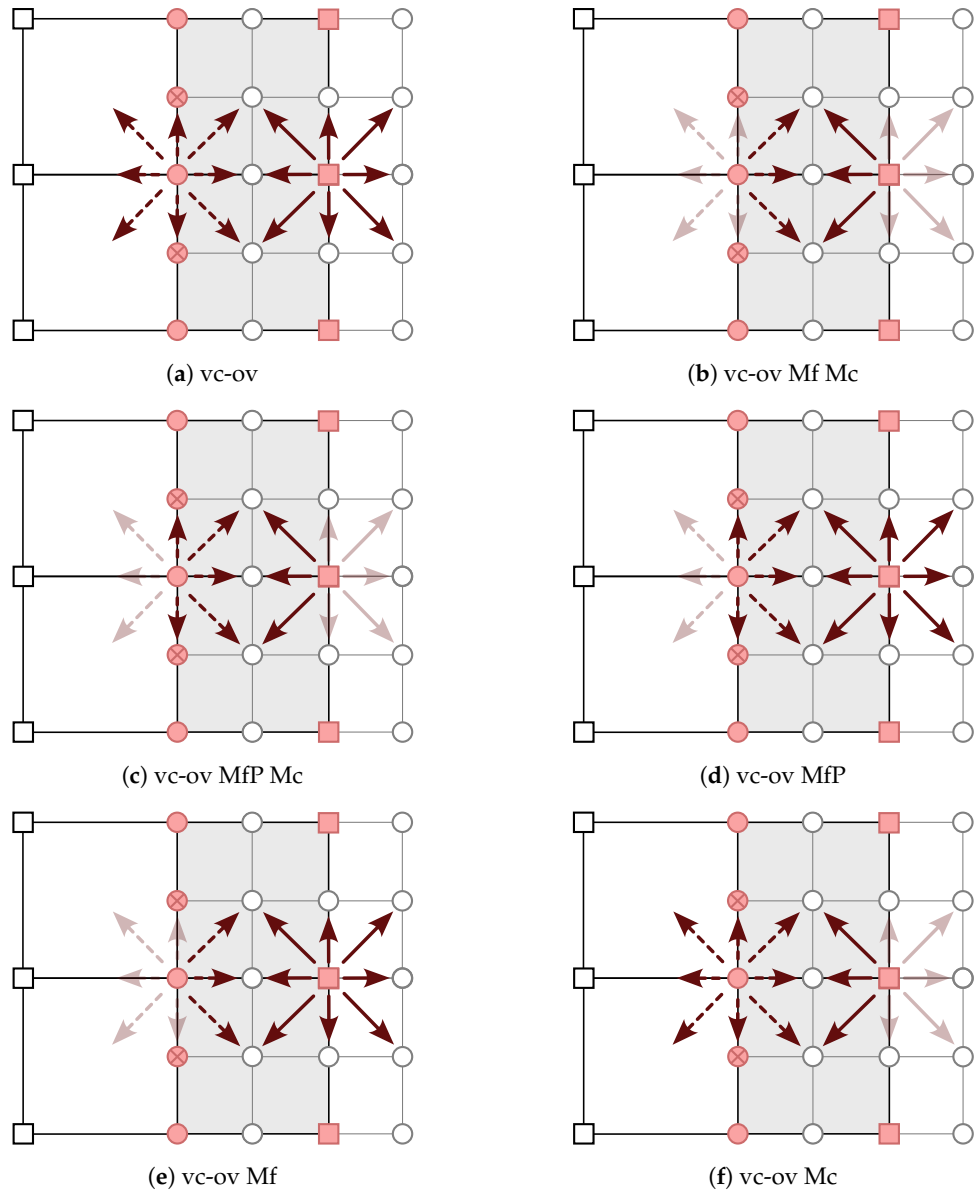


Figure A2. Schematic depiction of partial reconstruction variants based on the vc-ov grid interface. Opaque arrows: Distribution functions reconstructed during the grid communication step. Transparent

arrows: Known functions, retained during grid communication. Dashed arrow lines: Fine distribution functions. Solid arrow lines: Coarse distribution functions.

Appendix C

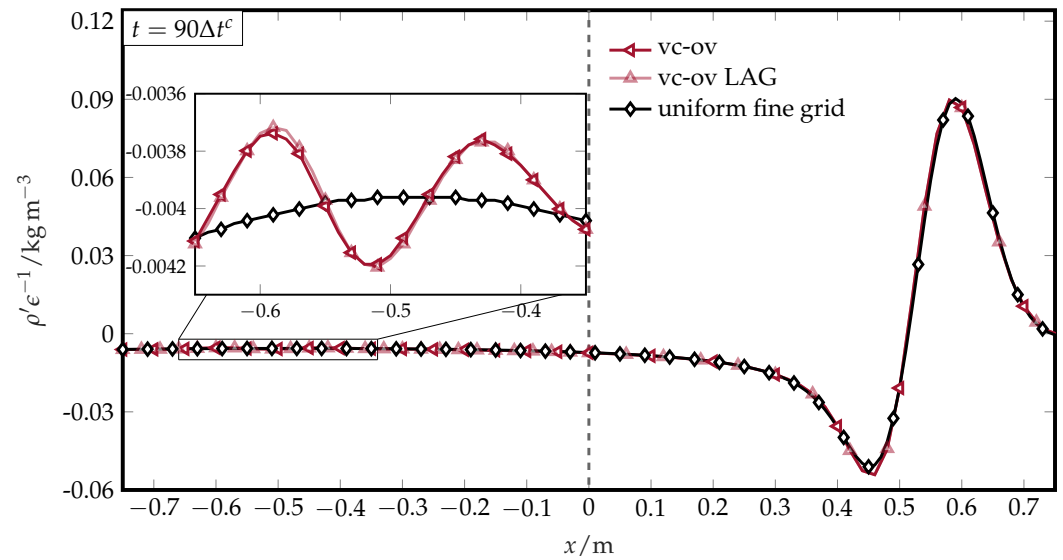


Figure A3. Gaussian acoustic pulse test case: Spurious reflection of the pulse at the GTI for vc-ov with and without LAG filter.

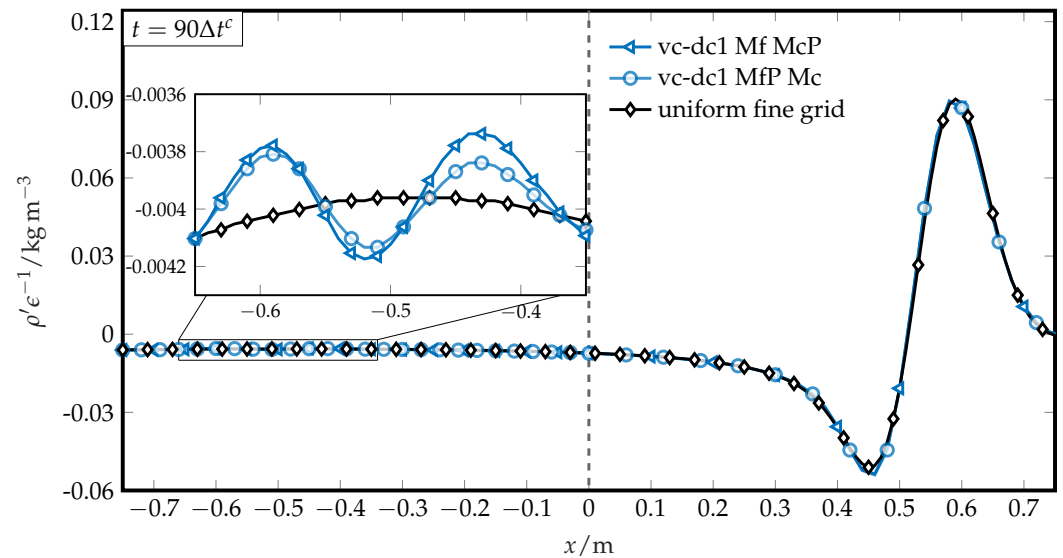


Figure A4. Spurious reflection of the Gaussian pulse at the GTI for vc-dc1. Retaining a maximum of coarse information during reconstruction at interface nodes noticeably reduces the reflection amplitude.

Appendix D

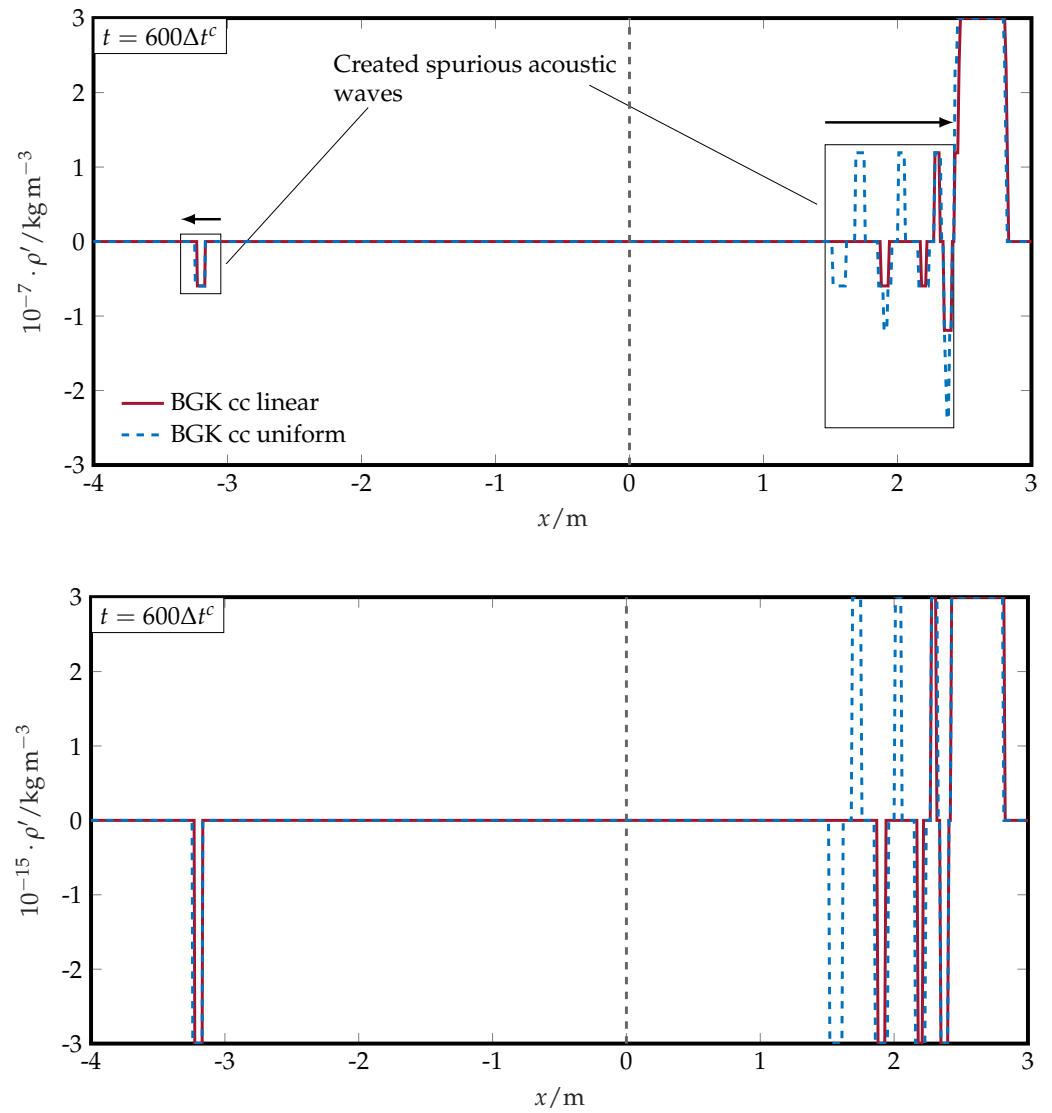


Figure A5. Convected acoustic wave test case: No up- and downstream acoustic waves are generated at the GTI due to the cc scheme’s mass conservation properties. The **upper** and **lower** diagrams differ in ordinate scaling.

Appendix E

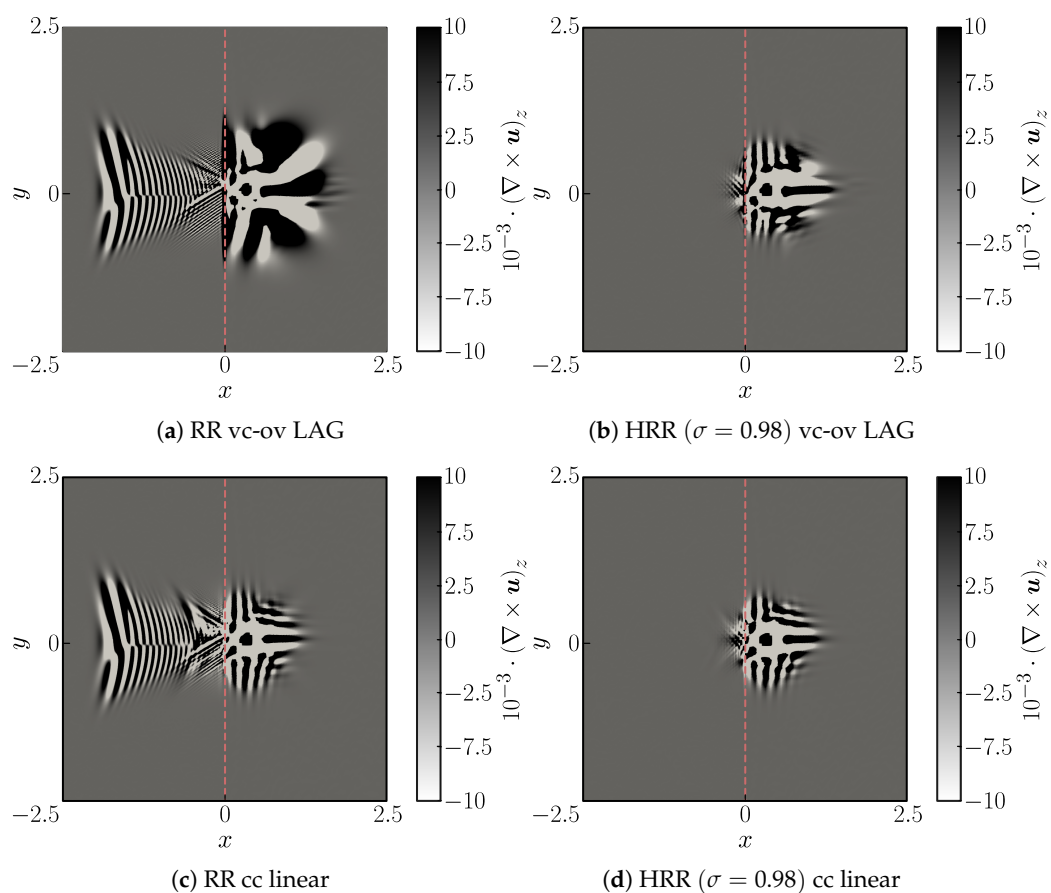


Figure A6. Top: Spurious shear mode amplification at the GTI resulting in strong deformation of the convected barotropic vortex for RR compared with HRR with vc-ov LAG at $t = 600\Delta t^f$. **Bottom:** No such phenomena appear with the cell-centered algorithm. Units: $[x] = \text{m}$, $[y] = \text{m}$, $[(\nabla \times \mathbf{u})_z] = \text{s}^{-1}$.

References

1. Ricot, D.; Marié, S.; Sagaut, P.; Bailly, C. Lattice Boltzmann method with selective viscosity filter. *J. Comput. Phys.* **2009**, *228*, 4478–4490.
2. Gendre, F.; Ricot, D.; Fritz, G.; Sagaut, P. Grid refinement for aeroacoustics in the lattice Boltzmann method: A directional splitting approach. *Phys. Rev. E* **2017**, *96*, 023311.
3. Astoul, T.; Wissocq, G.; Boussuge, J.F.; Sengissen, A.; Sagaut, P. Analysis and reduction of spurious noise generated at grid refinement interfaces with the lattice Boltzmann method. *J. Comput. Phys.* **2020**, *418*, 109645.
4. Astoul, T.; Wissocq, G.; Boussuge, J.F.; Sengissen, A.; Sagaut, P. Lattice Boltzmann method for computational aeroacoustics on non-uniform meshes: A direct grid coupling approach. *J. Comput. Phys.* **2021**, *447*, 110667.
5. Schukmann, A.; Schneider, A.; Haas, V.; Böhle, M. Analysis of Hierarchical Grid Refinement Techniques for the Lattice Boltzmann Method by Numerical Experiments. *Fluids* **2023**, *8*, 103.
6. Chen, H.; Teixeira, C.; Molvig, K. Realization of fluid boundary conditions via discrete Boltzmann dynamics. *Int. J. Mod. Phys. C* **1998**, *09*, 1281–1292.
7. Filippova, O.; Hänel, D. Grid Refinement for Lattice-BGK Models. *J. Comput. Phys.* **1998**, *147*, 219–228.
8. Dupuis, A.; Chopard, B. Theory and applications of an alternative lattice Boltzmann grid refinement algorithm. *Phys. Rev. E* **2003**, *67*, 066707.
9. Yu, D.; Mei, R.; Shyy, W. A multi-block lattice Boltzmann method for viscous fluid flows. *Numer. Methods Fluids* **2002**, *39*, 99–120.
10. Yu, D.; Mei, R.; Luo, L.S.; Shyy, W. Viscous flow computations with the method of lattice Boltzmann equation. *Prog. Aerosp. Sci.* **2003**, *39*, 329–367.
11. Crouse, B.; Rank, E.; Krafczyk, M.; Olke, J.T. A LB-based approach for adaptive flow simulations. *Int. J. Mod. Phys.* **2003**, *17*, 109–112.

12. Peng, Y.; Shu, C. Application of multi-block approach in the immersed boundary-lattice Boltzmann method for viscous fluid flows. *J. Comput. Phys.* **2006**, *218*, 460–478.
13. Lagrava, D.; Malaspinas, O.; Latt, J.; Chopard, B. Advances in multi-domain lattice Boltzmann grid refinement. *J. Comput. Phys.* **2012**, *231*, 4808–4822.
14. Touil, H.; Ricot, D.; Leveque, E. Direct and large-eddy simulation of turbulent flows on composite multi-resolution grids by the lattice Boltzmann method. *J. Comput. Phys.* **2013**, *256*, 220–233.
15. Rohde, M.; Kandhai, D.; Derksen, J.J.; van den Akker, H.E.A. A generic, mass conservative local grid refinement technique for lattice-Boltzmann schemes. *Int. J. Numer. Methods Fluids* **2006**, *51*, 439–468.
16. Chen, H.; Filippova, O.; Hoch, J.; Molvig, K.; Shock, R.; Teixeira, C.; Zhang, R. Grid refinement in lattice Boltzmann methods based on volumetric formulation. *Phys. A* **2006**, *362*, 158–167.
17. Kutscher, K.; Geier, M.; Krafczyk, M. Multiscale Simulation of Turbulent Flow interacting with Porous Media based on a massively parallel implementation of the Cumulant Lattice Boltzmann Method. *Comput. Fluids* **2018**, *193*, 103733.
18. Geier, M.; Greiner, A.; Korvink, J.G. Bubble functions for the lattice Boltzmann method and their application to grid refinement. *Eur. Phys. J. Spec. Top.* **2009**, *171*, 173–179.
19. Schönherr, M.; Kucher, K.; Geier, M.; Stiebler, M.; Freudiger, S.; Krafczyk, M. Multi-thread implementations of the lattice Boltzmann method on non-uniform grids for CPUs and GPUs. *Comput. Math. Appl.* **2011**, *61*, 3730–3743.
20. Vichnevetsky, R. Propagation through numerical mesh refinement for hyperbolic equations. *Math. Comput. Simul.* **1981**, *23*, 344–353.
21. Vichnevetsky, R. Propagation and spurious reflection in finite-element approximations of hyperbolic equations. *Comput. Math. Appl.* **1985**, *11*, 733–746.
22. Vichnevetsky, R.; Turner, L. Spurious scattering from discontinuously stretching grids in computational fluid dynamics. *Appl. Numer. Math.* **1991**, *8*, 289–299.
23. Visbal, M.R.; Gaitonde, D.V. On the use of high-order finite-difference schemes on curvilinear deforming meshes. *J. Comput. Phys.* **2002**, *181*, 155–185.
24. Vanella, M.; Piomelli, U.; Balaras, E. Effect of grid discontinuities on large-eddy simulation statistics and flow fields. *J. Turbul.* **2008**, *9*, N32.
25. Zhang, Q. High-order, multidimensional and conservative coarse-fine interpolation for adaptive mesh refinement. *Comput. Methods Appl. Mech. Eng.* **2011**, *200*, 3159–3168.
26. Thiele, F. Simulation of Airframe Noise Using a two-step DES/FWH approach. In Proceedings of the MUSAF II Colloquium, Toulouse, France, 18–20 September 2013.
27. Bras, S.L.; Deniau, H.; Bogey, C. A flux reconstruction technique for non-conforming grid interfaces in aeroacoustic simulations. In Proceedings of the AIAA/CEAS Aeroacoustics Conference, Lyon, France, 30 May–1 June 2016.
28. Hasert, M. Multi-Scale Lattice Boltzmann Simulations on Distributed Octrees. Ph.D. Thesis, RWTH Aachen, Aachen, Germany, 2013.
29. Pasquali, A. Developed a New LBM Grid Generator and a New LBM Wall Function (Based on OpenFOAM) for CFD Simulations on Multiple GPGPUs. Ph.D. Thesis, TU Braunschweig, Braunschweig, Germany, 2016.
30. Dawi, A. Compressible CFD Simulations of Aeroacoustics for Automotive Applications. Ph.D. Thesis, Technische Universität Braunschweig, Braunschweig, Germany, 2019.
31. Astoul, T. Towards Improved Lattice Boltzmann Aeroacoustic Simulations with Non-Uniform Grids: Application to Landing Gears Noise Prediction. Ph.D. Thesis, Aix-Marseille Université, Marseille, France, 2021.
32. Crouse, B.; Freed, D.; Balasubramanian, G.; Senthoooran, S.; Lew, P.T.; Mongeau, L. Fundamental Aeroacoustics Capabilities of the Lattice-Boltzmann Method. In Proceedings of the 12th AIAA/CEAS Aeroacoustics Conference (27th AIAA Aeroacoustics Conference), Cambridge, CA, USA, 8–10 May 2006; AIAA 2006-2571.
33. Lafitte, A.; Perot, F. Investigation of the Noise Generated by Cylinder Flows Using a Direct Lattice-Boltzmann Approach. In Proceedings of the 15th AIAA/CEAS Aeroacoustics Conference (30th AIAA Aeroacoustics Conference), Miami, FL, USA, 11–13 May 2009; AIAA 2009-3268.
34. Perot, F.; Kim, M.S.; Moreau, S.; Henner, M. Axial fan noise aeroacoustics predictions and inflow effect on tonal noise using LBM. In Proceedings of CFD Canada 2013, Sherbrooke, QC, Canada, 6–9 May 2013. Available online: https://www.researchgate.net/publication/287645676_Axial_fan_noise_aeroacoustics_predictions_and_inflow_effect_on_tonal_noise_using_LBM (accessed on 21 December 2024).
35. Sturm, M.; Sanjosé, M.; Moreau, S.; Carolus, T. Aeroacoustic Simulation of an Axial Fan Including the Full Test Rig by Using the Lattice Boltzmann Method. In Proceeding of the Fan 2015, Lyon, France, 15–17 April 2015. Available online: https://www.mb.uni-siegen.de/iftsm/forschung/veroeffentlichungen_pdf/149_2015.pdf (accessed on 21 December 2024).

36. Brionnaud, R.; Modena, M.C.; Trapani, G.; Holman, D.M. Direct Noise Computation with a Lattice-Boltzmann Method and Application to Industrial Test Cases. In Proceedings of the 22nd AIAA/CEAS Aeroacoustics Conference, Lyon, France, 30 May–1 June 2016; AIAA 2016-2969.
37. Feuchter, C. Direct aeroacoustic simulation with a cumulant Lattice-Boltzmann model. *Comput. Fluids* **2021**, *224*, 104970.
38. Jacob, J.; Malaspinas, O.; Sagaut, P. A new hybrid recursive regularised Bhatnagar-Gross-Krook collision model for Lattice Boltzmann method-based large eddy simulation. *J. Turbul.* **2018**, *19*, 1051–1076.
39. Höld, R.; Brenneis, A.; Eberle, A. Numerical Simulation of Aeroacoustic Sound Generated by Generic Bodies Placed on a Flat Plate: Part I—Prediction of Aeroacoustic Sources. In Proceedings of the AIAA/CEAS Aeroacoustics Conference, Bellevue, WA, USA, 10–12 May 1999; AIAA 1999-1896.
40. He, X.; Luo, L.S. A priori derivation of the lattice Boltzmann equation. *Phys. Rev. E* **1997**, *55*, R6333–R6336.
41. Shan, X.; Yuan, X.F.; Chen, H. Kinetic theory representation of hydrodynamics: A way beyond the Navier-Stokes equation. *J. Fluid Mech.* **2006**, *550*, 413–441.
42. Schneider, A. A Consistent Large Eddy Approach for Lattice Boltzmann Methods and its Application to Complex Flows. Ph.D. Thesis, Technical University of Kaiserslautern, Kaiserslautern, Germany, 2015.
43. Bhatnagar, P.L.; Gross, E.P.; Krook, M. A Model For Collision Processes in Gases. *Phys. Rev.* **1954**, *94*, 511–525.
44. Coreixas, C.; Chopard, B.; Latt, J. Comprehensive comparison of collision models in the lattice Boltzmann framework: Theoretical investigations. *Phys. Rev. E* **2019**, *100*, 033305.
45. Yoo, H.; Bahlali, M.L.; Favier, J.; Sagaut, P. A hybrid recursive regularized lattice Boltzmann model with overset grids for rotating geometries. *Phys. Fluids* **2021**, *33*, 057113.
46. Coreixas, C. High-Order Extension of the Recursive Regularized Lattice Boltzmann Method. Ph.D. Thesis, Université de Toulouse, Toulouse, France, 2018.
47. Lätt, J.; Chopard, B. Lattice Boltzmann method with regularized pre-collision distribution functions. *Math. Comput. Simul.* **2006**, *72*, 165–168.
48. Zhang, R.; Shan, X.; Chen, H. Efficient kinetic method for fluid simulation beyond the Navier-Stokes equation. *Phys. Rev. E* **2006**, *74*, 046703.
49. Malaspinas, O. Increasing stability and accuracy of the lattice Boltzmann scheme: Recursivity and regularization. *arXiv* **2015**, arXiv:1505.06900.
50. Renard, F.; Wissocq, G.; Boussuge, J.; Sagaut, P. A linear stability analysis of compressible hybrid lattice Boltzmann methods. *arXiv* **2020**, arXiv:2006.08477.
51. Wissocq, G.; Coreixas, C.; Boussuge, J.F. Linear stability and isotropy properties of athermal regularized lattice Boltzmann methods. *Phys. Rev. E* **2020**, *102*, 053305.
52. Izquierdo, S.; Martínez-Lera, P.; Fueyo, N. Analysis of open boundary effects in unsteady lattice Boltzmann simulations. *Comput. Math. Appl.* **2009**, *58*, 914–921.
53. Krüger, T.; Kusumaatmaja, H.; Kuzmin, A.; Shardt, O.; Silva, G.; Viggen, E.M. *The Lattice Boltzmann Method: Principles and Practice*; Graduate Texts in Physics; Springer: Berlin/Heidelberg, Germany, 2017.
54. Heubes, D.; Bartel, A.; Ehrhardt, M. Characteristic boundary conditions in the lattice Boltzmann method for fluid and gas dynamics. *J. Comput. Appl. Math.* **2014**, *262*, 51–61.
55. Poinot, T.J.; Lelef, S.K. Boundary conditions for direct simulations of compressible viscous flows. *J. Comput. Phys.* **1992**, *101*, 104–129.
56. Izquierdo, S.; Fueyo, N. Characteristic nonreflecting boundary conditions for open boundaries in lattice Boltzmann methods. *Phys. Rev. E* **2008**, *78*, 046707.
57. Jung, N.; Seo, H.W.; Yoo, C.S. Two-dimensional characteristic boundary conditions for open boundaries in the lattice Boltzmann methods. *J. Comput. Phys.* **2015**, *302*, 191–199.
58. Wissocq, G.; Gourdain, N.; Malaspinas, O.; Eyssartier, A. Regularized characteristic boundary condition for the Lattice Boltzmann methods at high Reynolds number flows. *J. Comput. Phys.* **2017**, *331*, 1–18.
59. Selle, L.; Nicoud, F.; Poinot, T. Actual Impedance of Nonreflecting Boundary Conditions: Implications for Computation of Resonators. *Am. Inst. Aeronaut. Astronaut. J.* **2004**, *42*, 958–964.
60. Lin, C.L.; Lai, Y.G. Lattice Boltzmann method on composite grids. *Phys. Rev. E* **2000**, *62*, 2219–2225.
61. Kirst, D. Historical Development of the Betatron. *Nature* **1946**, *157*, 90–95. <https://doi.org/10.1038/157090A0>.
62. Freudiger, S. Entwicklung Eines Parallelen, Adaptiven, Komponentenbasierten Strömungskerns für Hierarchische Gitter auf Basis des Lattice-Boltzmann-Verfahrens. Ph.D. Thesis, TU Braunschweig, Braunschweig, Germany, 2009.
63. Crouse, B. Lattice-Boltzmann Strömungssimulation auf Baumdatenstrukturen. Ph.D. Thesis, TU München, München, Germany, 2003.
64. Qi, J.; Klimach, H.; Roller, S. Implementation of the compact interpolation within the octree based Lattice Boltzmann solver Musubi. *Comput. Math. Appl.* **2019**, *78*, 1131–1141.

65. Li, Y.; Shan, X. Lattice Boltzmann method for adiabatic acoustics. *Phil. Trans. R. Soc.* **2011**, *369*, 2371–2380.
66. Song, Q.; Chen, R.; Cio, S.; Lou, J.; Zhan, N.; You, Y. A Simplified Linearized Lattice Boltzmann Method for Acoustic Propagation Simulation. *Entropy* **2022**, *24*, 1622.
67. van der Spek, P. GPU-accelerated Large Eddy Simulation of non-eutectic MSFR Salt Freezing in Turbulent Channel Flow. Master's Thesis, TU Delft, Delft, The Netherlands, 2024.
68. Berezin, A.; Perepelkina, A.; Ivanov, A.; Levchenko, V. Recalibration of LBM Populations for Construction of Grid Refinement with No Interpolation. *Fluids* **2023**, *8*, 179. <https://doi.org/10.3390/fluids8060179>.

Disclaimer/Publisher's Note: The statements, opinions and data contained in all publications are solely those of the individual author(s) and contributor(s) and not of MDPI and/or the editor(s). MDPI and/or the editor(s) disclaim responsibility for any injury to people or property resulting from any ideas, methods, instructions or products referred to in the content.